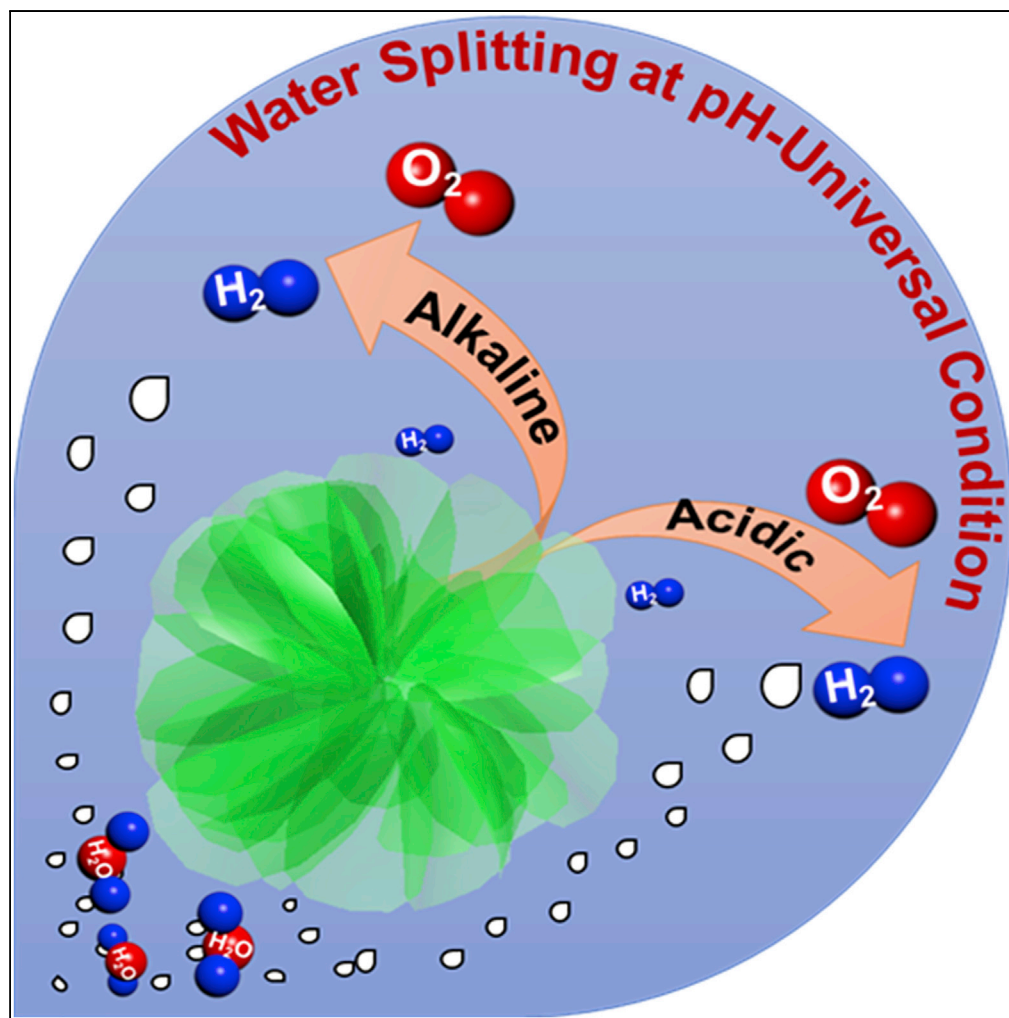**Article**

pH-Universal Water Splitting Catalyst: Ru-Ni Nanosheet Assemblies

Jian Yang, Qi Shao, Bolong Huang, Mingzi Sun, Xiaoqing Huang

bhuang@polyu.edu.hk (B.H.)
hxq006@suda.edu.cn (X.H.)

HIGHLIGHTS

A facile method for the synthesis of 3D hierarchical assembly Ru-Ni NA catalyst

Superior catalytic reactivity and stability of water splitting in universal pH

The introduction of Ni can modify the d-band and surface electronic environment

Minimization of the surface Coulomb repulsion leads to barrier-free catalysis process

Article

pH-Universal Water Splitting Catalyst: Ru-Ni Nanosheet Assemblies

Jian Yang,[1,3] Qi Shao,[1,3] Bolong Huang,[2,*] Mingzi Sun,[2] and Xiaoqing Huang[1,4,*]

SUMMARY

Although electrochemical water splitting is an effective and green approach to produce oxygen and hydrogen, the realization of efficient bifunctional catalysts that are stable in variable electrolytes is still a significant challenge. Herein, we report a three-dimensional hierarchical assembly structure composed of an ultrathin Ru shell and a Ru-Ni alloy core as a catalyst functioning under universal pH conditions. Compared with the typical Ir/C-Pt/C system, superior catalytic performances and excellent durability of the overall water splitting under universal pH have been demonstrated. The introduction of Ni downshifts the d-band center of the Ru-Ni electrocatalysts, modulating the surface electronic environment. Density functional theory results reveal that the mutually restrictive d-band interaction lowers the binding of (Ru, Ni) and (H, O) for easier O-O and H-H formation. The structure-induced eg-dz^2 misalignment leads to minimization of surface Coulomb repulsion to achieve a barrier-free water-splitting process.

INTRODUCTION

Hydrogen (H$_2$) is becoming increasingly important as a future fuel compared with fossil fuels because of its advantages of clean and renewable energy generation (Dresselhaus and Thomas, 2001; Turner, 2004). Electrochemical water splitting provides an effective approach for H$_2$ production. Water splitting consists of the hydrogen evolution reaction (HER) and oxygen evolution reaction (OER), both of which require efficient catalysts to reduce the overpotential for practical applications (Jin et al., 2015; Zhang et al., 2017a; Balogun et al., 2016). Although platinum (Pt) is regarded as a conventional HER catalyst in acidic solutions owing to its highest exchange current density and low Tafel slope, it shows an "incomparable" HER activity in alkaline solutions owing to the sluggish reaction kinetics (Ma et al., 2017; Mahmood et al., 2017; Zheng et al., 2016). Even though non-noble metal materials have been widely explored as enhanced catalysts for HER, the greatest challenge for the use of non-noble metal materials so far is that their HER activities still underperform Pt-based catalysts, and they are susceptible to acid corrosion (Zhang et al., 2017b; Conway and Tilak, 2002). Similar obstacles are still unavoidable for non-noble metal materials for OER applications owing to their relatively high overpotentials for driving the OER process and the low energy conversion efficiencies. To date, pursuit of effective catalysts for both OER and HER in the same electrolyte, not to mention under universal pH conditions, has been extremely desirable (Zheng et al., 2014; Wang et al., 2018a, 2018b; Ellis et al., 2010). Therefore, the development of efficient and stable bifunctional catalysts for the simultaneous production of H$_2$ and oxygen (O$_2$) under universal pH conditions is still a significant challenge.

It has been generally considered that noble metal materials, such as Ru-based catalysts, are the most promising catalysts for use as overall water-splitting catalysts owing to their promising activities for the two half-reactions in both acidic and alkaline solutions as well as their high stability under extreme conditions (Lu et al., 2014; Jin et al., 2016; Petrykin et al., 2010; Seitz et al., 2016; Kong et al., 2016). However, the water-splitting performances of the reported Ru-based catalysts are still far from satisfactory, particularly under universal pH conditions. From the viewpoint of the structure, a two-dimensional (2D) structure can provide great opportunities for enhancing the electrochemical performance because it largely exposes the surface area (Hang et al., 2014; Gao et al., 2012). However, undesirable drawbacks arise from the severe aggregation or fracture that usually occurs during the electrochemical process, inevitably leading to the obvious activity decay. This renders the conventional 2D structure not an ideal candidate for efficient electrocatalysis (Zheng et al., 2014; Chhowalla et al., 2013; Hwang et al., 2011; Chen et al., 2015). Based on this, the assembly of 2D structures into unique 3D structures may provide an effective strategy to achieve efficient catalysts for water splitting under universal pH conditions because the structures can achieve a large exposure of the active sites while stabilizing the structure.

[1]College of Chemistry, Chemical Engineering and Materials Science, Soochow University, Suzhou, Jiangsu 215123, China

[2]Department of Applied Biology and Chemical Technology, The Hong Kong Polytechnic University, Hung Hom, Kowloon, Hong Kong SAR

[3]These authors contributed equally

[4]Lead Contact

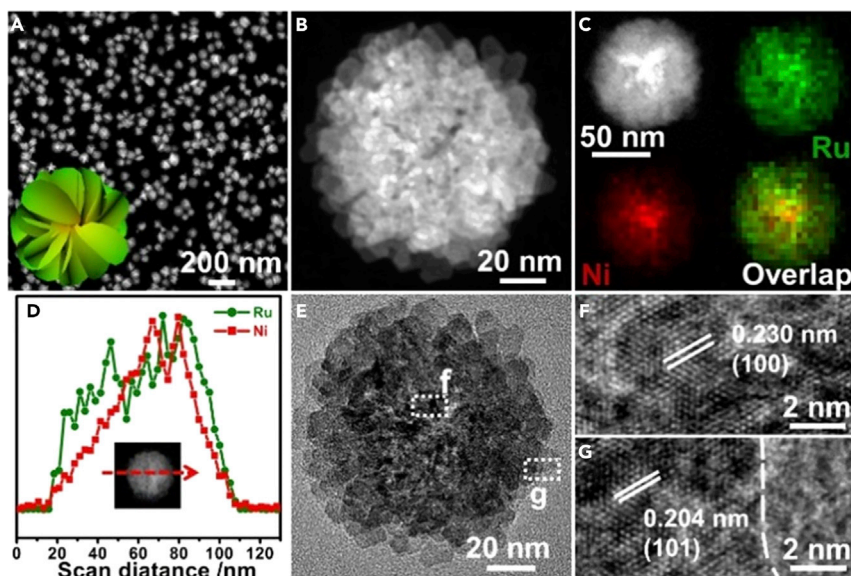*Correspondence: bhuang@polyu.edu.hk (B.H.), hxq006@suda.edu.cn (X.H.)

Figure 1. Structural Characterizations of the Ru_3Ni_3 NAs

(A–G) (A and B) HAADF-STEM image, (C) HAADF-STEM image and elemental mapping, (D) line scans, (E) TEM image, and (F and G) high-resolution TEM images of the Ru_3Ni_3 NAs.

RESULTS

Synthesis and Characterization of Ru-Ni NAs

To surmount this challenge, we report an efficient wet chemical approach for the synthesis of 3D hierarchical Ru-Ni nanosheet assemblies (NAs) consisting of ultrathin nanosheets as subunits and explore their high performances for overall water splitting under universal pH conditions. The distinctive hierarchical NA structures are highly beneficial for enhancing electrochemical energy conversion. We found that the introduction of Ni into Ru largely downshifts the d-band center of the Ru-Ni NAs and effectively modulates the surface environment for HER. After air treatment at 350°C, the newly generated abundant RuO_2 provides effective active sites for OER. As a result, the Ru-Ni NAs deliver high HER and OER activities as well as outstanding stability under a broad range of pH conditions. More interestingly, Ru_3Ni_3 NAs demonstrated potential applications for overall water splitting with a lower overpotential, smaller Tafel slope, and better stability than the reference Ir/C-Pt/C catalyst.

A typical preparation of Ru-Ni NAs was introduced by adding ruthenium(III) acetylacetonate ($Ru(acac)_3$), nickel(II) acetylacetonate ($Ni(acac)_2$), phloroglucinol, tetramethylammonium bromide, polyvinylpyrrolidone (PVP), and benzyl alcohol into a glass vial. After capping the vial, the mixture was ultrasonicated for approximately 1 h. The resulting homogeneous mixture was then heated from room temperature to 160°C and maintained at 160°C for 5 h using an oil bath. Ru-Ni NAs with different Ru/Ni ratios (i.e., Ru_3Ni_3 NAs, Ru_3Ni_2 NAs, and Ru_3Ni_1 NAs) have been readily achieved by tuning the Ru/Ni precursor amount ratios (Figures S1A–S1C).

The detailed characterizations of Ru_3Ni_3 NAs were further carried out to determine the 3D assembly structure (Figures 1, S1D, and S1E). The high-angle annular dark-field scanning transmission electron microscopic (HAADF-STEM) image (Figure 1A) showed at first glance that all the products had a spherical outline, which indicated the high purity of product. For a close view of the Ru_3Ni_3 NAs, enlarged HAADF-STEM was performed, and a 3D flower-like structure assembled by hierarchical 2D nanosheet subunits was clearly observed (Figure 1B). Elemental mappings and line scans showed that the flower-like Ru_3Ni_3 NAs had a typical core-shell structure consisting of a Ru-Ni core and Ru shell (Figures 1C and 1D). Compared with those of the pure Ru NAs, additional X-ray diffraction (XRD) peaks in the Ru-Ni alloy were observed for 3D Ru_3Ni_3 NAs, which further confirmed the core-shell structure of the Ru_3Ni_3 NAs with the Ru phase and Ru-Ni alloy phase (Figures S1D and S1E). As revealed by the high-resolution transmission electron microscopic (TEM) image of the Ru_3Ni_3 NAs, lattice fringes with interplanar distances of

0.204 and 0.230 nm were observed, which correlated well with the (101) plane of Ru and the (100) plane of the Ru-Ni alloy, respectively (Figures 1E–1G).

Notably, the morphologies of Ru$_3$Ni$_2$ NAs and Ru$_3$Ni$_1$ NAs with different Ru/Ni ratios were similar (Figures S2A, S2B, S2E, S2H, S2I, and S2L). The XRD results show that as the amount of Ni increased, the main peaks of the Ru-Ni alloy approach the standard pure Ni XRD peaks (PCPDS No. 89–7,129), which suggested the successful alloying of Ni into Ru. The energy dispersive spectroscopy (EDS) elemental mapping images and line scans confirm that the alloys have a core-shell structure similar to that of the Ru$_3$Ni$_3$ NAs (Figures S2C, S2D, S2J, and S2K). The same lattice fringes with an interplanar distance of 0.204 nm were found in the Ru$_3$Ni$_2$ NAs and Ru$_3$Ni$_1$ NAs, which correlated well to the (101) plane of Ru. Lattice fringes of the (100) Ru-Ni alloy with interplanar distances of 0.231 and 0.232 nm were also observed in the Ru$_3$Ni$_2$ NAs and Ru$_3$Ni$_1$ NAs, respectively (Figures S2F, S2G, S2M, and S2N).

The direct creation of unique, 3D Ru-Ni superstructures with ultrathin building blocks is the most striking feature of the synthesis reported here, which has never been reported previously. To gain a better understanding of the growth mechanism behind the successful synthesis, characterizations of the intermediates collected at different reaction times were also carefully performed (Figures S3A–S3J). At the beginning of the reaction (25 min), intermediates with messy and irregular multi-branched structures were observed (Figures S3A and S3B). Nanosheets began to form, and a portion of the assembled flower-shaped intermediates appeared at a reaction time of 40 min (Figures S3C and S3D). When the reaction reached 1.5 h, the diameter of the flower-shaped intermediates increased (Figures S3E and S3F). After the reaction progressed for 3 h, the monodispersed, hierarchical assembly became obvious (Figures S3G and S3H). A further increase in the size of the Ru$_3$Ni$_3$ NAs was observed after the completion of the reaction (Figures S3I and S3J). The different reaction intermediates were also further analyzed by XRD (Figure S4), and the peaks of Ru and small peaks of the Ru-Ni alloy were detected during the initial 25 min. With the prolonged reaction time, the peak indexed to the Ru-Ni alloy became increasingly obvious and shifted to a higher angle, which indicated that more Ni was reduced and alloyed with Ru (Figure S3K).

To further understand the formation progress behind the successful synthesis, the effect of various experimental parameters on the morphology of Ru-Ni NAs was carried out. The results reveal that the combined use of PVP, phloroglucinol, and tetramethylammonium bromide was essential for the successful creation of Ru-Ni NAs. The Ru-Ni NAs could not be obtained in the absence of any PVP or phloroglucinol (Figures S5A, S5B, S7A, and S7B). Further detailed control experiments show that high-quality Ru-Ni NAs could only be obtained in the presence of specific amount of phloroglucinol and tetramethylammonium bromide. For example, irregular morphology was obtained when the amounts of phloroglucinol and tetramethylammonium bromide were changed (Figures S5 and S6), and a layered product with low yield was obtained when benzyl alcohol was replaced by ethylene glycol (Figures S7C and S7D). The morphology of assemblies has changed greatly without using Ni(acac)$_2$ (Figure S8).

HER Performance of Ru-Ni NAs

Considering that Ru is expected to have high activities for HER and OER, the design of Ru-based catalysts for overall water splitting is highly significant from the viewpoint of practical applications (Pu et al., 2017; Jiang et al., 2015), but the systematic study of Ru-based catalysts is still very limited, especially in a broad pH range. To this end, detailed HER and OER measurements were carried out in electrolytes with different pH values using Ru-Ni NAs as the candidate catalyst. All electrochemical measurements were performed in a standard three-electrode system with a saturated calomel electrode as the reference electrode and a carbon rod as the counter electrode. The reference electrodes were calibrated before the electrochemical measurements (Figure S9). All polarization curves were recorded without iR compensation. Before the electrocatalytic measurements, all different Ru-Ni NAs were loaded on a carbon support (Vulcan XC72R carbon) by sonication. Ru loading of 20 wt % was maintained in each catalyst, and no obvious morphological changes were observed after heat treatment (Figure S10). The resulting Ru-Ni NAs/C were then dispersed in a mixture solvent containing isopropanol and Nafion (5%) and sonicated for 30 min to form a homogeneous catalyst ink. The concentration of the Ru-Ni NAs loading on the carbon powder was controlled at 2 mg mL^{-1}; 10 μL catalyst ink was uniformly dropped onto a glassy carbon electrode and dried naturally at room temperature.

The HER performance of the Ru-Ni NAs/C was first explored at a slow scan rate of 5 mV s^{-1} to ensure steady-state behavior on the electrode surface. To obtain the best performance of the Ru-Ni NAs/C in
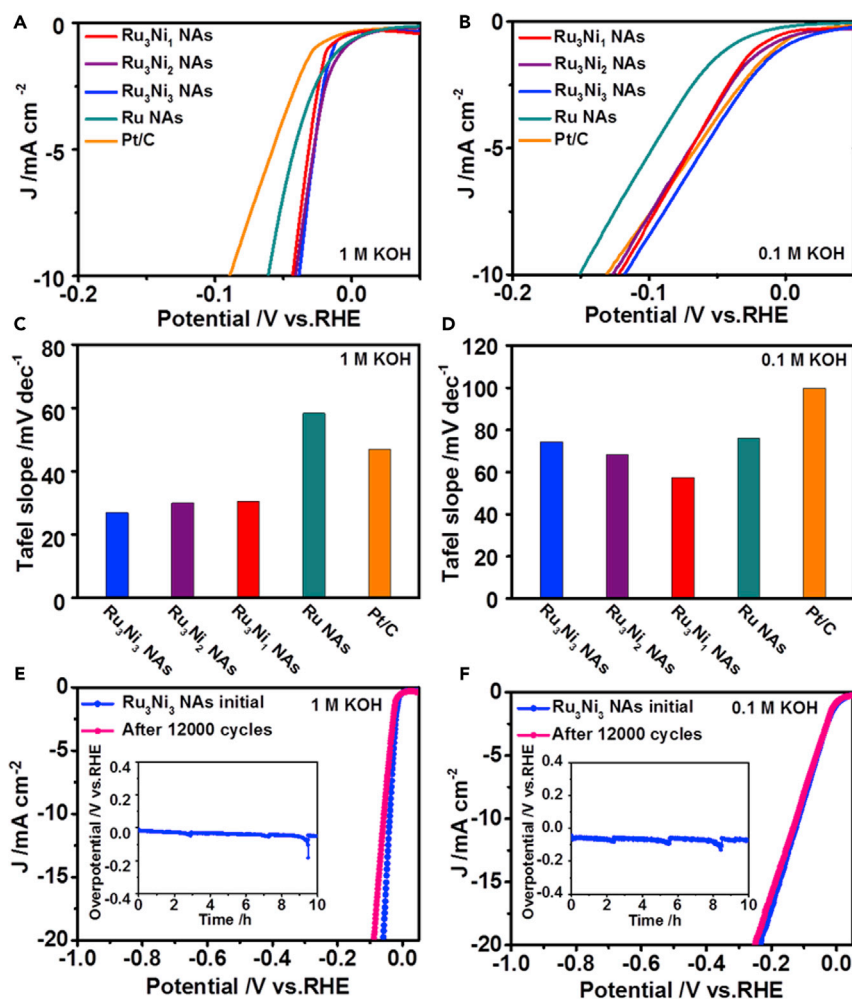
Figure 2. HER Performances of the Ru$_3$Ni$_3$ NAs, Ru$_3$Ni$_2$ NAs, Ru$_3$Ni$_1$ NAs, Ru NAs, and Pt/C under Different Alkaline Conditions

(A and C) (A) The polarization curves and (C) corresponding Tafel plots in 1 M KOH.

(B and D–F) (B) The polarization curves and (D) corresponding Tafel plots in 0.1 M KOH. Scan rate is 5 mV s^{-1}. Polarization curves of the Ru$_3$Ni$_3$ NAs before and after 12,000 cycles in (E) 1 M KOH and (F) 0.1 M KOH solutions at a scan rate of 5 mV s^{-1}. Insets: chronopotentiometry curves of the Ru$_3$Ni$_3$ NAs in 1 M KOH and 0.1 M KOH solutions at a constant current density of 5 mA cm^{-2}.

HER, we first determined the effects of the annealing temperature and atmosphere on HER performance by using Ru$_3$Ni$_3$ NAs as the candidate material. As shown in Figures S11A and S11B, the sample annealed at 250°C for 1 h exhibited the best HER activity in both alkaline and acidic conditions (0.5 M H$_2$SO$_4$ and 1 M KOH solutions). Figure 2A shows the polarization curves of the Ru-Ni NAs and Ru NAs and commercial Pt/C in 1 M KOH. In detail, at a current density of 10 mA cm^{-2}, the overpotentials of Ru$_3$Ni$_3$ NAs, Ru$_3$Ni$_2$ NAs, Ru$_3$Ni$_1$ NAs, Ru NAs, and commercial Pt/C were 39, 42, 44, 62, and 90 mV, respectively, versus the reversible hydrogen electrode (RHE), and the Ru$_3$Ni$_3$ NAs showed the smallest value. The Tafel slope is an intrinsic property of the catalyst that is determined by the rate-limiting step of the HER (Cherevko et al., 2016). Importantly, the Tafel slopes of the Ru$_3$Ni$_3$ NAs, Ru$_3$Ni$_2$ NAs, and Ru$_3$Ni$_1$ NAs were calculated to be 26.9, 29.9, and 30.5 mV dec^{-1}, respectively (Figures 2C and S12A). In contrast, the Ru NAs and commercial Pt/C showed relatively high Tafel slopes of 58.3 mV dec^{-1} and 46.8 mV dec^{-1}. The electrocatalytic stability of the Ru$_3$Ni$_3$ NAs was further studied by both long-term cycling and chronopotentiometry tests, and the polarization curves of Ru$_3$Ni$_3$ NAs exhibited no obvious change after 12,000 cycles (Figure 2E). The Ru$_3$Ni$_3$ NAs showed only a slight potential increase after 10 h of chronopotentiometry at a current density of 5 mA cm^{-2} (Figure 2E, inset).

With the change in the electrolyte to 0.1 M KOH, the Ru-Ni NAs still showed promising HER activities. At 10 mA cm^{-2}, the overpotentials of the Ru$_3$Ni$_3$ NAs, Ru$_3$Ni$_2$ NAs, Ru$_3$Ni$_1$ NAs, Ru NAs, and commercial Pt/C were 119, 127, 123, 152, and 132 mV, respectively (Figure 2B). In addition to the low overpotentials, the Ru$_3$Ni$_3$ NAs, Ru$_3$Ni$_2$ NAs, and Ru$_3$Ni$_1$ NAs also exhibited lower Tafel slopes than Pt/C (99.7 mV dec^{-1}) and Ru NAs (76.0 mV dec^{-1}) (Figures 2D and S12B). The Ru$_3$Ni$_3$ NAs also exhibited excellent durability after 12,000 cycles and in the chronopotentiometry test in 0.1 M KOH (Figure 2F), which indicated that the Ru$_3$Ni$_3$ NAs exhibit a superior HER activity and durability under alkaline conditions.

The HER properties of the Ru-Ni NAs under acidic conditions were further investigated. Figure S13 shows that the overpotentials of the Ru$_3$Ni$_3$ NAs, Ru$_3$Ni$_2$ NAs, Ru$_3$Ni$_1$ NAs, and Ru NAs were 39 and 96 mV, 39 and 115 mV, 46 and 112 mV, and 55 and 122 mV at a current density of 10 mA cm^{-2} in 0.5 M H$_2$SO$_4$ and 0.05 M H$_2$SO$_4$, respectively. The Tafel slopes of the Ru$_3$Ni$_3$ NAs, Ru$_3$Ni$_2$ NAs, Ru$_3$Ni$_1$ NAs, and Ru NAs were 53.9 and 67.1 mV dec^{-1}, 53.5 and 64.0 mV dec^{-1}, 54.2 and 66.8 mV dec^{-1}, and 81.6 and 79.6 mV dec^{-1} in 0.5 M H$_2$SO$_4$ and 0.05 M H$_2$SO$_4$, respectively. The Ru-Ni NAs showed a much better HER performance than the Ru NAs, indicating the vital role of Ni in improving the HER performance. After the working electrode was cycled for 6,000 cycles, the Ru$_3$Ni$_3$ NAs exhibited the best durability under acidic conditions with potential increases of only 62 and 39 mV in 0.5 M H$_2$SO$_4$ and 0.05 M H$_2$SO$_4$, respectively. In addition, after the 12-h chronopotentiometry test at 5 mA cm^{-2} in 0.5 M H$_2$SO$_4$ and 0.05 M H$_2$SO$_4$, the Ru$_3$Ni$_3$ NAs showed only potential increases of 36 and 49 mV, respectively (Figures S13E and S13F).

OER Performances of Ru-Ni NAs

The obtained Ru-Ni NAs were also successfully applied as efficient OER catalysts. Before the OER tests, the Ru-Ni NAs were also subjected to thermal annealing in air at different temperatures because Ru oxide has been discovered to be an active component for the OER (Petrykin et al., 2010; Reier et al., 2012). As shown in Figures S11C and S11D, the catalyst after heat treatment in air (350°C, 2 h) showed the best performance under both acidic and alkaline conditions (0.5 M H$_2$SO$_4$ and 1 M KOH). The TEM images show that the hierarchical structures were largely preserved (Figures S10C and S10D). We also studied the structural characterization of NAs after heat treatment by STEM image, elemental mapping, and line scan, where the core-shell structures of Ru$_3$Ni$_3$ NAs are largely reserved (Figure S14). We also showed that the carbon can enhance both the electrical conductivity and the dispersion of Ru$_3$Ni$_3$ NAs, and thus improve the electrocatalysis (Figure S15). To evaluate the OER performances of Ru-Ni under universal pH conditions, we tested the OER performances in both acidic (0.5 and 0.05 M H$_2$SO$_4$) and alkaline (1 and 0.1 M KOH) electrolytes. The commercial Ir/C catalyst was chosen as the reference because Ir is considered to be the benchmark catalyst for OER (Lettenmeier et al., 2016; Zhang et al., 2017c).

Examination of the OER polarization curves in 0.5 and 0.05 M H$_2$SO$_4$ shows that the Ru-Ni NAs showed much better OER activities than the Ru NAs and commercial Ir/C. To drive a current density of 10 mA cm^{-2}, the Ru$_3$Ni$_3$ NAs, Ru$_3$Ni$_2$ NAs, and Ru$_3$Ni$_1$ NAs required overpotentials of 252 mV, 260 mV, and 268 mV in 0.5 M H$_2$SO$_4$, respectively (Figure 3A). The Tafel slopes of the Ru$_3$Ni$_3$ NAs, Ru$_3$Ni$_2$ NAs, and Ru$_3$Ni$_1$ NAs derived from Figure 3A were 45.8, 46.1, and 46.0 mV dec^{-1} in 0.5 M H$_2$SO$_4$, respectively. In contrast, the commercial Ir/C and Ru NAs required larger overpotentials of 328 and 277 mV in 0.5 M H$_2$SO$_4$, respectively. The Tafel slopes of the commercial Ir/C and Ru NAs were also larger than those of the Ru-Ni NAs (Figures 3C and S16A). Similar trends were also obtained in 0.05 M H$_2$SO$_4$, and the Ru$_3$Ni$_3$ NAs showed the lowest overpotential and Tafel slope of 312 mV and 70.8 mV dec^{-1}, respectively (Figures 3B, 3D, and 6B).

We further measured the OER activities in different alkaline electrolytes. The overpotentials of the Ru$_3$Ni$_3$ NAs, Ru$_3$Ni$_2$ NAs, and Ru$_3$Ni$_1$ NAs were 304, 309, and 301 mV in 1 M KOH, whereas the Ru NAs and commercial Ir/C showed larger overpotentials of 351 and 311 mV, respectively (Figure S17A). The Tafel slopes of the Ru$_3$Ni$_3$ NAs, Ru$_3$Ni$_2$ NAs, Ru$_3$Ni$_1$ NAs, Ru NAs, and commercial Ir/C derived from Figure S15A were 91.7, 67.9, 73.4, 111.1, and 47.1 mV dec^{-1}, respectively (Figure S17C). When the solution is replaced by a dilute alkaline solution (0.1 M KOH), in which it is more difficult for the OER to proceed (Lu and Zhao, 2015), the Ru-Ni NAs also exhibited a high activity. The overpotentials of the Ru$_3$Ni$_3$ NAs, Ru$_3$Ni$_2$ NAs, and Ru$_3$Ni$_1$ NAs were 394, 390, and 384 mV, respectively, which were smaller than those of the Ru NAs (439 mV) and commercial Ir/C (407 mV) (Figure S17B). The Tafel slopes of the Ru$_3$Ni$_3$ NAs, Ru$_3$Ni$_2$ NAs, Ru$_3$Ni$_1$ NAs, Ru NAs, and commercial Ir/C derived from Figure S17B were 133.8, 131.4, 130.2, 140.7, and 111.1 mV dec^{-1}, respectively (Figure S17D). All these results confirmed that the unique Ru-Ni NAs show
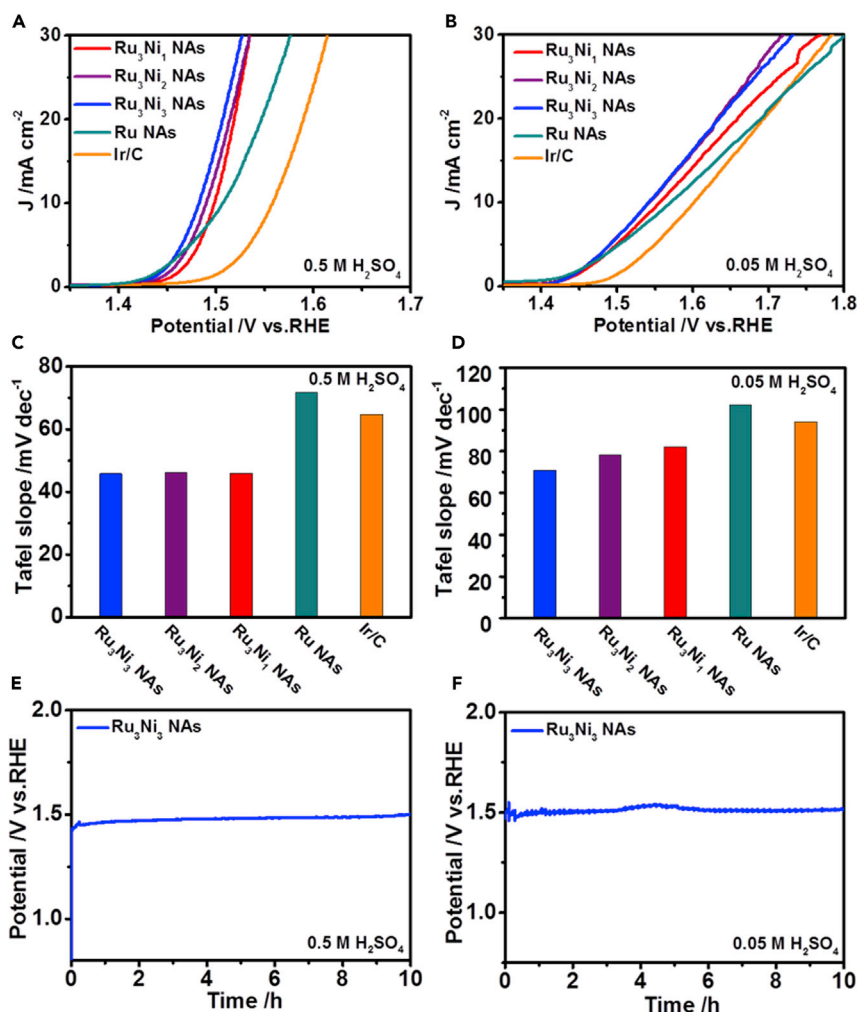
CellPress

Figure 3. OER Performances of the Ru_3Ni_3 NAs, Ru_3Ni_2 NAs, Ru_3Ni_1 NAs, Ru NAs, and Commercial Ir/C under Different Acidic Conditions

(A and C) (A) The polarization curves and (C) corresponding Tafel plots in 0.5 M H_2SO_4.

(B and D–F) (B) The polarization curves and (D) corresponding Tafel plots in 0.05 M H_2SO_4. Scan rate is 5 mV s^{-1}. Chronopotentiometry curves of the Ru_3Ni_3 NAs in (E) 0.5 M H_2SO_4 and (F) 0.05 M H_2SO_4 solutions at a current density of 5 mA cm^{-2}.

excellent OER performances compared with the Ru NAs. In addition, in the 10-h chronopotentiometry test, the Ru_3Ni_3 NAs showed limited degradation after continuous electrolysis at 5 mA cm^{-2} in 0.5 M H_2SO_4, 0.05 M H_2SO_4, 1 M KOH, and 0.1 M KOH (Figures 3E, 3F,S17E, and S17F). No obvious morphological changes were observed in 0.5 M H_2SO_4 and 1 M KOH after the chronopotentiometry test (Figure S18), which demonstrated that the Ru-Ni NAs are indeed "acidic- and alkaline-stable" OER catalysts. To further demonstrate the OER and HER stability, chronopotentiometry test at higher current density was also performed, where the Ru_3Ni_3 NAs still showed limited degradations after continuous OER and HER electrolysis at 10 mA cm^{-2} in 0.5 M H_2SO_4 and 1 M KOH (Figure S19).

Water-Splitting Performance of the Ru-Ni NAs

As we explored the best catalysts for HER and OER under both acidic and alkaline conditions, a two-electrode setup with anodic catalyst Ru_3Ni_3 NAs after air treatment at 250°C for 1 h and cathodic catalyst Ru_3Ni_3 NAs after air treatment at 350°C for 2 h was used to study the potential application of Ru-Ni NAs in overall water splitting under universal pH conditions. The Linear Sweep Voltammetry (LSV) plots of Ru_3Ni_3 NAs and Ir/C-Pt/C under different pH conditions are presented in Figure 4A. The data clearly show that
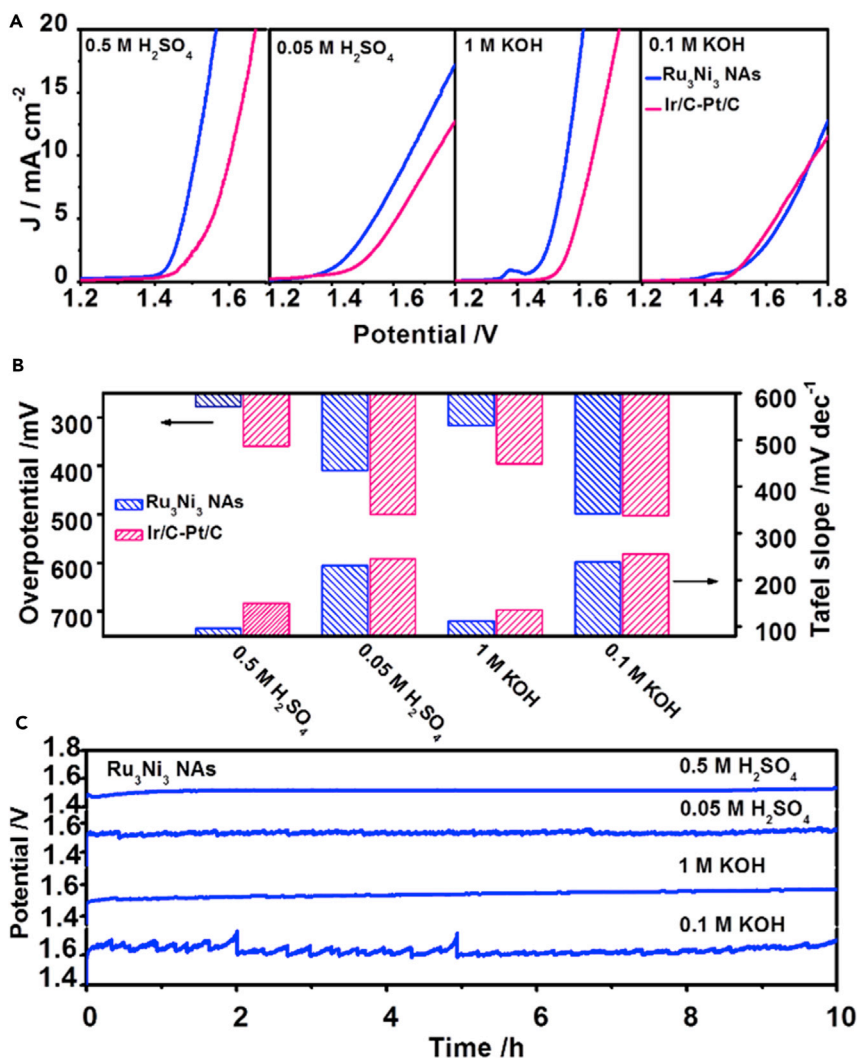
Figure 4. Overall Water Splitting Performances of the Ru-Ni NAs under Different pH Conditions

(A and B) (A) Polarization curves for the overall water splitting and (B) the overpotentials and Tafel plots of the Ru_3Ni_3 NAs and Ir/C-Pt/C in 0.5 M H_2SO_4, 0.05 M H_2SO_4, 1 M KOH, and 0.1 M KOH.

(C) Chronopotentiometry curves of the Ru_3Ni_3 NAs in 0.5 M H_2SO_4, 0.05 M H_2SO_4, 1 M KOH, and 0.1 M KOH at a constant current density of 5 mA cm^{-2}.

both the potentials and Tafel slopes of the Ru_3Ni_3 NAs are much lower than those of Ir/C-Pt/C. The Ru_3Ni_3 NAs show an overpotential of 280 mV in 0.5 M H_2SO_4, which is considerably lower than that of Ir/C-Pt/C (370 mV). The Tafel slope of the Ru_3Ni_3 NAs is only 96.9 mV dec^{-1}, whereas that of Ir/C-Pt/C is as high as 150.1 mV dec^{-1} (Figures 4B and S20A), indicating that the reaction kinetics of the Ru_3Ni_3 NAs are much faster than those of Ir/C-Pt/C. Significantly, the Ru_3Ni_3 NAs showed excellent durability with limited degradation after a 10-h chronopotentiometry test at 5 mA cm^{-2} in 0.5 M H_2SO_4, 0.05 M H_2SO_4, 1 M KOH, and 0.1 M KOH (Figure 4C). Overall, these results confirmed that the Ru-Ni NAs can serve as excellent water-splitting catalysts under universal pH conditions.

DISCUSSIONS

It should be noted that both the HER and OER activities of the Ru-Ni NAs in different electrolytes are higher than those of most catalysts reported to date (Tables S1–S3). To explore the reasons behind the high performance, the surface structures of the different catalysts were first explored in detail. As shown in Figure S10, no obvious morphological changes were found in the Ru-Ni NAs after heat treatment. However, the XRD peaks assigned to RuO_2 appeared in the catalysts processed at 350°C in air, and the
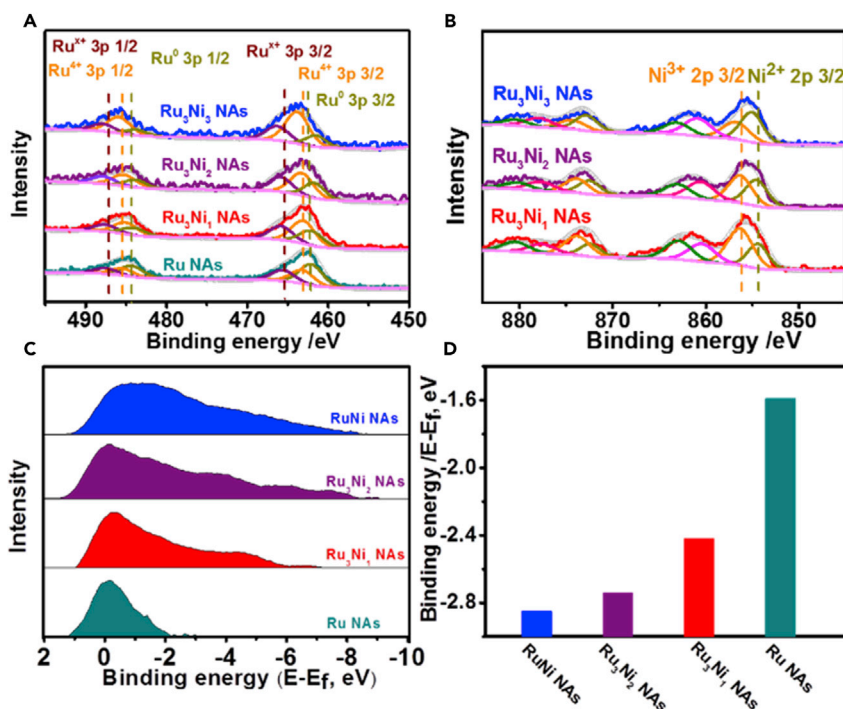
Figure 5. XPS Analysis of the Ru_3Ni_3 NAs, Ru_3Ni_2 NAs, Ru_3Ni_1 NAs, and Ru NAs

(A and B) (A) Ru 3p and (B) Ni 2p curves of the Ru_3Ni_3 NAs, Ru_3Ni_2 NAs, Ru_3Ni_1 NAs, and Ru NAs heated at 350°C in air for 2 h.
(C and D) (C) Surface valence band photoemission spectra and (D) corresponding d-band centers of the Ru_3Ni_3 NAs, Ru_3Ni_2 NAs, Ru_3Ni_1 NAs, and Ru NAs heated at 250°C in air for 1 h.

Ru_3Ni_3 NAs showed the highest peak for RuO_2 (Figure S21A). Considering that RuO_2 plays an important role in enhancing the OER activity, the formed RuO_2 greatly enhances the OER activity in the Ru-Ni NAs (Fang and Liu, 2010). XPS was also carried out to explore the surface properties of the Ru-Ni NAs. Figure S22 shows the full scan curves of the different Ru-Ni NAs, and the positions of the Ru and Ni peaks were consistent with the literature results (Folkesson et al., 1973). Furthermore, the XPS peaks of Ru in different catalysts after treatment at 350°C in air for 2 h were divided into Ru 3p3/2 and Ru 3p1/2 peaks, which can be further split into three peaks, corresponding to Ru^{x+} (purple line), Ru^{4+} (orange line), and Ru^0 (dark yellow line) (Figure 5A) (Li et al., 2016). It was calculated that the Ru^{4+} fractions in the Ru_3Ni_3 NAs (57.00%), Ru_3Ni_2 NAs (44.46%), and Ru_3Ni_1 NAs (44.57%) were much higher than those in the Ru NAs (29.89%) (Table S4), which confirmed the higher concentrations of RuO_2 in the Ru-Ni NAs. As shown in Figure 5B, the Ni 2p peaks in the Ru_3Ni_3 NAs, Ru_3Ni_2 NAs, and Ru_3Ni_1 NAs were composed of Ni 2p1/2 and Ni 2p3/2 peaks, which both split into two oxidized Ni peaks, namely, Ni^{2+} (dark yellow line) and Ni^{3+} (orange line) (Zhang et al., 2007; Gong and Dai, 2015). Ni^{3+} is helpful for the formation of NiOOH on the catalyst surface, resulting in a better OER performance (Lee et al., 2012). This result indicates that both Ru and Ni in high oxidation states are generated in the Ru-Ni NAs by treatment at 350°C for 2 h in air, and that they are beneficial for the enhanced OER performance.

Compared with the peaks of Ru-Ni NAs treated at 350°C for 2 h in air, no additional peaks were generated for the Ru-Ni NAs treated at 250°C for 1 h in air (Figure S21B). Based on XPS analysis, Ru can be successfully split into three peaks, namely, Ru^{x+} (purple line), Ru^{4+} (orange line), and Ru^0 (dark yellow line) (Figure S23). It was calculated that the area ratios of the metallic Ru0 were 59.74%, 56.77%, and 58.06% in the Ru_3Ni_3 NAs, Ru_3Ni_2 NAs, and Ru_3Ni_1 NAs, respectively, which were higher than 56.08% in the Ru NAs. (Table S5) and indicated a large number of active sites of metallic Ru present on the surface of the Ru_3Ni_3 NAs. Surface valence band XPS spectra were also obtained to determine the d-band centers of the Ru-Ni NAs treated at 250°C in air (Figures 5C and 5D). The d-band center downshifted with the increasing concentration of Ni. The reported d-band centers of Pt and Ru are located at −2.32 and −1.49 eV, respectively, corresponding to hydrogen binding energies of −0.32 and −0.64 eV, respectively, and suggesting that Ru shows a stronger hydrogen adsorption than Pt (Jiao et al., 2015). Pt is regarded as the best catalyst for HER performance

owing to the suitable binding energy between the catalysts and adsorbates. Here, by alloying the catalyst with Ni, a downshift of the d-band center was observed in the Ru-Ni NAs (Figures 5C and 5D), which results in a suitable binding energy between the Ru-Ni NAs and adsorbates and boosted the HER activity of the Ru-Ni NAs (Stamenkovic et al., 2007).

We further carried out density functional theory (DFT) calculations to elucidate how the downshift effect of the Ru-Ni NAs is related to the high performance of water splitting for both the OER and HER. The Ru-Ni NA system was modeled by a hexagonal lattice (hex-Ru-Ni) based on the Ru local symmetry. It shows a good metallic behavior with uniform isotropic conductivity across the Fermi level (E_F) (Figure 6A). The d-orbital projected density of states (PDOS) were compared and showed that Ni-3d downshifted to a value lower than that obtained for the bulk face-centered cubic Ni metal (Figure 6B) due to repulsion with the overlapping Ru-4d orbital, which implied a weakening in the Ni-O and Ni-H bonding. In addition, this downshifting effect appeared to be even more pronounced within the hexagonal local lattice than in the cubic lattice. Meanwhile, the Ru-4d states also downshifted compared with those in the hex-Ru metal, especially for the 4d-e_g component above the E_F (Figure 6B), regardless of the different local symmetries. This occurs because the eg-level component is essential for the adsorption of the bond of the p-π lone pair electrons in molecules such as H_2O, O, or O_2. This is because they almost remain in the non-bonding orbitals, and the adsorption stabilities are dominated by the Coulomb repulsion between 4d-e_g in such p-π orbitals. Accordingly, the Ru in hex-Ru-Ni will easily transfer electrons between the catalysis substrate and intermediate molecules and facilitate O-O bond formation. The simulated OER pathway (Figure 6C) shows that the system is an energetically favorable catalyst even under U = 0 and U = 1.23 V, showing that water splitting with such Ru-Ni NAs would be a substantially low-barrier process. The splitting of H_2O results in an increase in energy of 1.49 eV, guaranteeing that the initiation would be very reactive within a low overpotential. Meanwhile, there is no evident change in the energy for the evolution reaction [HO*+(H$^+$+e$^-$)]→[O*+2(H$^+$+e$^-$)] (~0.4 eV). An additional similarly energetic increase (1.50 eV) was found for the formation of *OOH, indicating that the O* on the Ru-Ni still stays active to oxidize OH under lower overpotential. The splitting of H for the [HOO*+3(H$^+$+e$^-$)]→[O$_2$+4(H$^+$+e$^-$)] transformation is very active. Compared with the pathway at U = 1.23 V, we confirm the overall overpotential (i.e., η = max{[[barrier-1.23 eV]/e = 0.306 V}) is almost the same within the range of 0.200–0.300 V. Further calculations of the O_2 dissociation confirmed that the combined O-O on the Ru-contained surface will be easily dissociated and enter into the surrounding solution conditions (Figure S24, Tables S6 and S7). Therefore, the OER on the Ru-Ni surface can achieve a very high performance supported by an energetic barrier-free water-splitting process. We further gain energetic insights on the alkaline HER. In the Ru-Ni surface system without partial oxidations by O-coverage, the alkaline HER performance overall is energetically downhill and the whole process gains a reaction heat of −0.48 eV with a small barrier of 0.16 eV. Activation barrier for the HER on this system may arise due to barrier of [H_2O→H + OH]. As found by our experimental observation, partial oxidation states were found on the surface. We further conducted the reaction energy calculation. The overall reaction heat released is found to be −0.97 eV, showing it to be rather more energetically favorable than the case without oxidation. The process of [H_2O→H + OH] is also energetically preferred gaining −0.28 eV during the bond cleavage on the partially oxidized Ru-Ni surface (Figure 6D). At the same time, a comparison of the chemisorption energies sheds light on the high HER/OER performance (Figure 6E). We also determined that the HER on the Ru-Ni system favors high H coverage with easy chemisorption of the 2H, and the formation of 2H→H_2 is energetically favorable. Meanwhile, the low O coverage will easily facilitate water splitting and further accelerate further 2O chemisorption and O_2 desorption. The kinetics of possible oxygen absorption or oxygen-related intermediates (OH$^-$) is shown in absorption process in Figure 6F, which will result in the formation an intermediate distorted octahedral unit. The overlapping between eg orbital of Ru^{2+} and O-p$_\sigma$ orbitals will facilitate the ion transfer. The distorted structure prompts Ru^{2+} (d^6) to change from a low-spin state ($t_{2g}^6 e_g^0$) to an intermediate-spin state ($t_{2g}^5 e_g^1$), where the eg^1 can point to the intermediate with high bonding possibility. We also find that the absorption energy of further absorption on vertical oxygen molecule will be lowered nearly 1 eV, which can be attributed to the Jahn-Teller effect from the extra oxygen molecule to the c-axis of the distorted octahedral unit, which decreases the whole energy. Electrons on t_{2g} can be further excited to eg and then form a high-spin state ($t_{2g}^4 e_g^2$) with energy decrease. Overall, the Ru-Ni catalytic system is found to be efficient in HER performance from acidic to the basic condition. Thus, the Ru-Ni (NAs) system exhibits a high catalytic reactivity for water splitting based on the DFT calculations. We have also made a detail comparison for the preliminary absorption behavior on the cubic Ru-Ni (111) and hexagonal close packed (hcp) Ru-Ni (001) surface to elucidate the experimental treatment and
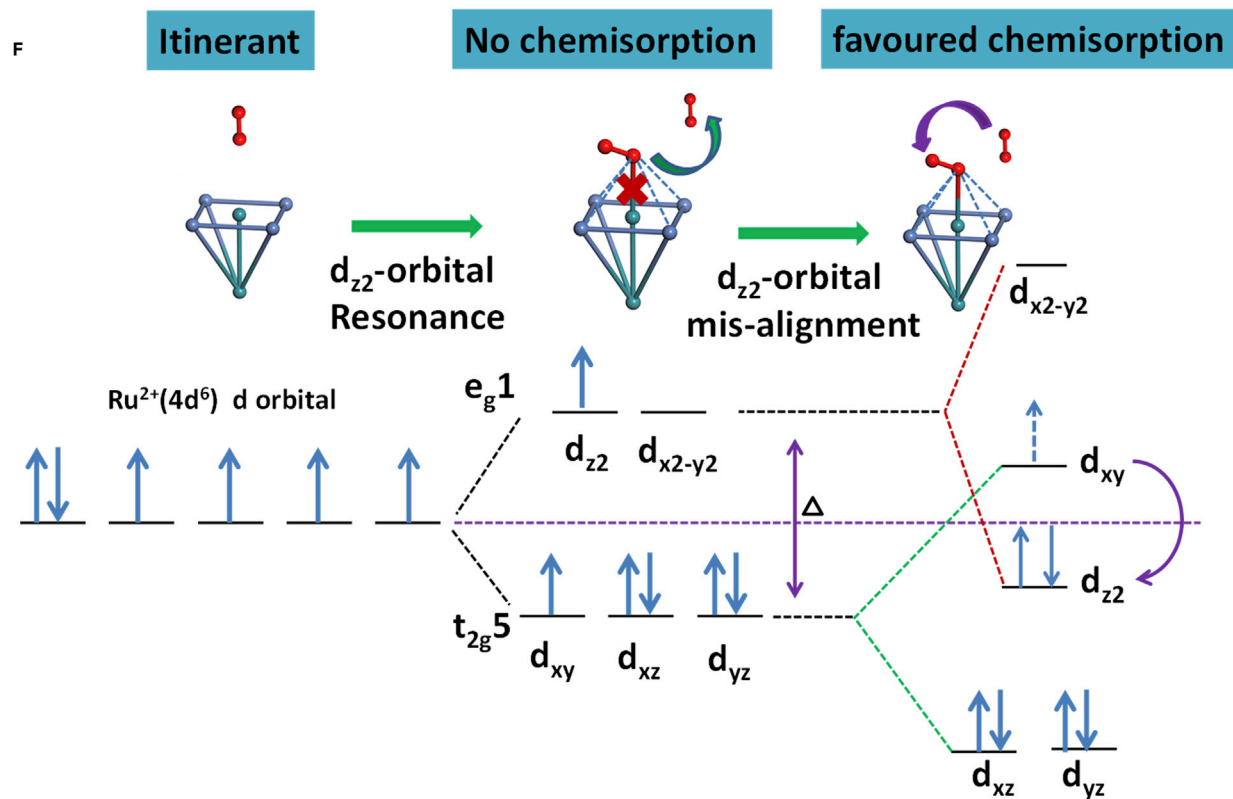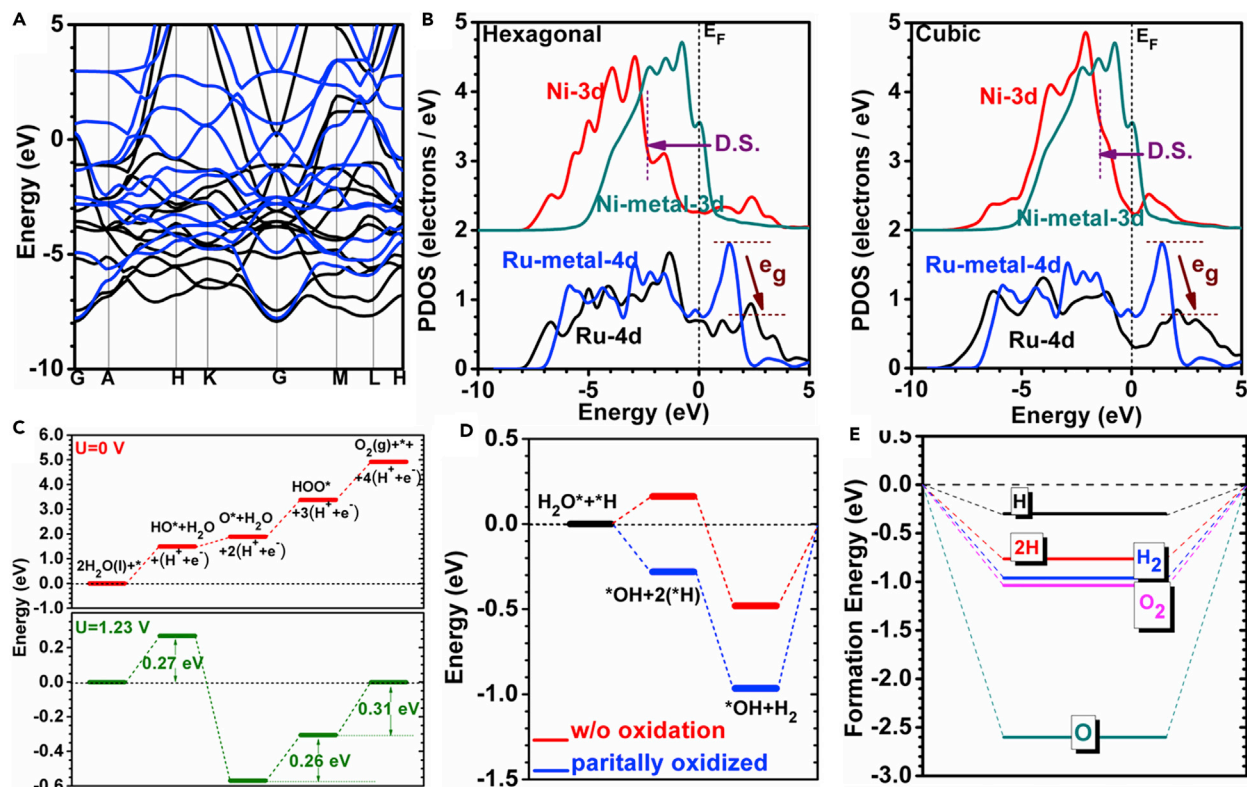
Figure 6. DFT Simulations of OER and HER

(A) The simulated band structure for the Ru-Ni hexagonal alloy.

(B) The PDOS of Ru-Ni.

(C) Free energy path for the OER.

(D) Free energy path for alkaline HER.

(E) The chemisorption energy for the acidic HER and neutral OER.

(F) Schematic illustration of the transition of electrons from t_{2g} to e_g orbital and the evolution of intermediate spin state to high spin state on Ru-Ni (100) surface. Green ball, Ru; blue ball, Ni; red ball, oxygen molecule.

related analysis. The discussions and analysis cover the following sections: energetics, electronic structures, orbital energetic behaviors, and adsorption analysis (Figures S24–S28 in Supplemental Information).

In summary, for the first time, we have demonstrated a facile method for the synthesis of 3D Ru-Ni NAs, which leads to favorable 3D Ru-Ni superstructures with fully exposed active sites. The valence band spectra and DFT calculations revealed a change in the d-band center in the Ru-Ni NAs after the introduction of Ni, resulting in the transformation to a favorable surface environment for the OER and HER. The RuO_2-decorated Ru-Ni NAs treated at 350°C in air provided additional active sites for the OER. The combined structural and electronic engineering leads to superior electrocatalytic performance for overall water splitting under universal pH conditions, and the performance is much better than that of the commercial Pt/C and Ir/C, demonstrating an unprecedented class of nanocatalysts with exceptional activity and excellent stability for electrochemical water splitting.

Limitations of the Study

Our work has demonstrated a novel bifunctional catalyst for water splitting in the universal environment from experimental and theoretical perspectives. Based on the combination of XPS and DFT as an effective approach, electronic environment modulation has been interpreted as the key factor that facilitates both HER and OER. However, an in-depth understanding of the oxidation states of the catalyst is still an open challenge because of the complex charge transfer induced by the overlap between the metal orbitals as well as the correspondingly accurate characterization. The site-to-site sampling and analysis of surface oxidation sites is of great significance for precise understanding of the catalyst reactivity. Therefore, we will keep working on further development and perfection on related theoretical exploration and advancement.

METHODS

All methods can be found in the accompanying Transparent Methods supplemental file.

SUPPLEMENTAL INFORMATION

Supplemental Information includes Transparent Methods, 28 figures, and 7 tables and can be found with this article online at https://doi.org/10.1016/j.isci.2019.01.004.

AUTHOR CONTRIBUTIONS

X.H. conceived and supervised the research. X.H., J.Y. and Q.S. designed the experiments. X.H., J.Y., and Q.S. performed most of the experiments and data analysis. X.H., J.Y., and Q.S. participated in various aspects of the experiments and discussions. B.H. and M.S. performed the DFT simulations. X.H., Q.S., J.Y., B.H., and M.S. wrote the paper. All authors discussed the results and commented on the manuscript.

DECLARATION OF INTERESTS

The authors declare no competing interests.

REFERENCES

Balogun, M.-S., Qiu, W., Yang, H., Fan, W., Huang, Y., Fang, P., Li, G., Ji, H., and Tong, Y. (2016). A monolithic metal-free electrocatalyst for oxygen evolution reaction and overall water splitting. Energy Environ. Sci. 9, 3411–3416.

Chen, S., Liu, G., Yadegari, H., Wang, H., and Qiao, S.Z. (2015). A Three-dimensional MnO2 ultrathin nanosheet aerogels for high-performance Li-O2 batteries. J. Mater. Chem. 3, 2559–2563.

Cherevko, S., Geiger, S., Kasian, O., Kulyk, N., Grote, J.-P., Savan, A., Shrestha, B.R., Merzlikin, S., Breitbach, B., Ludwig, A., and Mayrhofer, K.J.J. (2016). Oxygen and hydrogen evolution reactions on Ru, RuO2, Ir, and IrO2 thin film electrodes in acidic and alkaline electrolytes: a comparative study on activity and stability. Catal. Today 262, 170–180.

Chhowalla, M., Shin, H.S., Eda, G., Li, L.-J., Loh, K.P., and Zhang, H. (2013). The chemistry of two-dimensional layered transition metal dichalcogenide nanosheets. Nat. Chem. 5, 263–275.

Conway, B.E., and Tilak, B.V. (2002). Interfacial processes involving electrocatalytic evolution and oxidation of H2, and the role of chemisorbed H. Electrochim. Acta 47, 3571–3594.

Dresselhaus, M.S., and Thomas, I.L. (2001). Alternative energy technologies. Nature 414, 332–337.

Ellis, W.C., McDaniel, N.D., Bernhard, S., and Collins, T.J. (2010). Fast water oxidation using iron. J. Am. Chem. Soc. 132, 10990–10991.

Fang, Y.-H., and Liu, Z.-P. (2010). Mechanism and Tafel lines of electro-oxidation of water to oxygen on RuO2 (110). J. Am. Chem. Soc. 132, 18214–18222.

Folkesson, B., Bjorøy, M., Pappas, J., Skaarup, S., Aaltonen, R., and Swahn, C.G. (1973). ESCA studies on the charge distribution in some dinitrogen complexes of rhenium, iridium, ruthenium, and osmium. Acta Chem. Scand. 27, 287–302.

Gao, Q., Giordano, C., and Antonietti, M. (2012). Biomimetic oxygen activation by MoS2/Ta3N5 nanocomposites for selective aerobic oxidation. Angew. Chem. Int. Ed. 51, 11740–11744.

Gong, M., and Dai, H. (2015). A mini review of NiFe-based materials as highly active oxygen evolution reaction electrocatalysts. Nano Res. 8, 23–39.

Hang, L., Wu, H.B., Yan, Y., Wang, X., and Lou, X.W. (2014). Hierarchical MoS2 microboxes constructed by nanosheets with enhanced electrochemical properties for lithium storage and water splitting. Energy Environ. Sci. 7, 3302–3306.

Hwang, H., Kim, H., and Cho, J. (2011). MoS2 nanoplates consisting of disordered graphene-like layers for high rate lithium battery anode materials. Nano Lett. 11, 4826–4830.

Jiang, Y., Li, X., Yu, S., Jia, L., Zhao, X., and Wang, C. (2015). Reduced graphene oxide-modified carbon nanotube/polyimide film supported MoS2 nanoparticles for electrocatalytic hydrogen evolution. Adv. Funct. Mater. 25, 2693–2700.

Jiao, Y., Zheng, Y., Jaroniec, M., and Qiao, S.Z. (2015). Design of electrocatalysts for oxygen-and hydrogen-involving energy conversion reactions. Chem. Soc. Rev. 44, 2060–2086.

Jin, H., Wang, J., Su, D., Wei, Z., Pang, Z., and Wang, Y. (2015). In situ cobalt-cobalt oxide/N-vdoped carbon hybrids as superior bifunctional electrocatalysts for hydrogen and oxygen evolution. J. Am. Chem. Soc. 137, 2688–2694.

Jin, Y., Wang, H., Li, J., Yue, X., Han, Y., Shen, P.K., and Cui, Y. (2016). Porous MoO2 nanosheets as non-noble bifunctional electrocatalysts for overall water splitting. Adv. Mater. 28, 3785–3790.

Kong, X., Xu, K., Zhang, C., Dai, J., Norooz Oliaee, S., Li, L., Zeng, X., Wu, C., and Peng, Z. (2016). Free-standing two-dimensional Ru nanosheets with high activity toward water splitting. ACS Catal. 6, 1487–1492.

Lee, Y., Suntivich, J., May, K.J., Perry, E.E., and Shao-Horn, Y. (2012). Synthesis and activities of rutile IrO2 and RuO2 nanoparticles for oxygen evolution in acid and alkaline solutions. J. Phys. Chem. Lett. 3, 399–404.

Lettenmeier, P., Wang, L., Golla-Schindler, U., Gazdzicki, P., Cañas, N.A., Handl, M., Hiesgen, R., Hosseiny, S.S., Gago, A.S., and Friedrich, K.A. (2016). Nanosized IrOx-Ir catalyst with relevant activity for anodes of proton exchange membrane electrolysis produced by a cost-effective procedure. Angew. Chem. Int. Ed. 55, 742–746.

Li, X., Liu, J., Huang, Q., Vogel, W., Akins, D.L., and Yang, H. (2016). Effect of heat treatment on stability of gold particle modified carbon supported Pt-Ru anode catalysts for a direct methanol fuel cell. Electrochim. Acta 56, 278–284.

Lu, X.Y., and Zhao, C.E. (2015). Electrodeposition of hierarchically structured three-dimensional nickel-iron electrodes for efficient oxygen evolution at high current densities. Nat. Commun. 6, 6616.

Lu, Z.Y., Wang, H.T., Kong, D.S., Yan, K., Hsu, P.C., Zheng, G.Y., Yao, H.B., Liang, Z., Sun, X.M., and Cui, Y. (2014). Electrochemical tuning of layered lithium transition metal oxides for improvement of oxygen evolution reaction. Nat. Commun. 5, 4345.

Ma, Y.-Y., Wu, C.-X., Feng, X.-J., Tan, H.-Q., Yan, L.-K., Liu, Y., Kang, Z.-H., Wang, E.-B., and Li, Y.-G. (2017). Highly efficient hydrogen evolution from seawater by a low-cost and stable CoMoP@C electrocatalyst superior to Pt/C. Energy Environ. Sci. 10, 788–798.

Mahmood, J., Li, F., Jung, S.-M., Okyay, M.S., Ahmad, I., Kim, S.-J., Park, N., Jeong, H.Y., and Baek, J.-B. (2017). An efficient and pH-universal ruthenium-based catalyst for the hydrogen evolution reaction. Nat. Nanotechnol. 12, 441–446.

Petrykin, V., Macounova, K., Shlyakhtin, O.A., and Krtil, P. (2010). Tailoring the selectivity for electrocatalytic oxygen evolution on ruthenium oxides by zinc substitution. Angew. Chem. Int. Ed. 49, 4813–4815.

Pu, Z., Amiinu, I.S., Kou, Z., Li, W., and Mu, S. (2017). RuP2-based catalysts with platinum-like activity and higher durability for hydrogen evolution reaction at all pH value. Angew. Chem. Int. Ed. 56, 11559–11564.

Reier, T., Oezaslan, M., and Strasser, P. (2012). Electrocatalytic oxygen evolution reaction (OER) on Ru, Ir, and Pt catalysts: a comparative study of nanoparticles and bulk materials. ACS Catal. 2, 1765–1772.

Seitz, L.C., Dickens, C.F., Nishio, K., Hikita, Y., Montoya, J., Doyle, A., Kirk, C., Vojvodic, A., Hwang, H.Y., Norskov, J.K., and Jaramillo, T.F. (2016). A highly active and stable IrOx/SrIrO3 catalyst for the oxygen evolution reaction. Science 353, 1011–1014.

Stamenkovic, V.R., Fowler, B., Mun, B.S., Wang, G., Ross, P.N., Lucas, C.A., and Marković, N.M. (2007). Improved oxygen reduction activity on Pt3Ni (111) via increased surface site availability. Science 315, 493–497.

Turner, J.A. (2004). Sustainable hydrogen production. Science 305, 972–974.

Wang, X., Zhuang, L., He, T., Jia, Y., Zhang, L., Yan, X., Gao, M., Du, A., Zhu, Z., Yao, X., and Yu, S.-H. (2018a). Grafting cobalt diselenide on defective graphene for enhanced oxygen evolution reaction. iScience 7, 145–153.

Wang, X., Zhuang, L., Jia, Y., Liu, H., Yan, X., Zhang, L., Yang, D., Zhu, Z., and Yao, X. (2018b). Plasma-triggered synergy of exfoliation, phase

transformation, and surface engineering in cobalt diselenide for enhanced water oxidation. Angew. Chem. Int. Ed. 57, 16421–16425.

Zhang, J., Wang, H., and Dalai, A.K. (2007). Development of stable bimetallic catalysts for carbon dioxide reforming of methane. J. Catal. 249, 300–310.

Zhang, J., Wang, T., Liu, P., Liao, Z., Liu, S., Zhuang, X., Chen, M., Zschech, E., and Feng, X. (2017a). Efficient hydrogen production on MoN$_{i4}$ electrocatalysts with fast

water dissociation kinetics. Nat. Commun. 8, 15437.

Zhang, N., Shao, Q., Pi, Y., Guo, J., and Huang, X. (2017b). Solvent-mediated shape tuning of well-defined rhodium nanocrystals for efficient electrochemical water splitting. Chem. Mater. 29, 5009–5015.

Zhang, Y., Xia, X., Cao, X., Zhang, B., Tiep, N.H., He, H., Chen, S., Huang, Y., and Fan, H.J. (2017c). Ultrafine metal nanoparticles/N-doped porous carbon hybrids coated on carbon fibers as flexible and binder-free water

splitting catalysts. Adv. Energy Mater. 7, 1700220.

Zheng, Y., Jiao, Y., Zhu, Y., Li, L.H., Han, Y., Chen, Y., Du, A., Jaroniec, M., and Qiao, S.Z. (2014). Hydrogen evolution by a metal-free electrocatalyst. Nat. Commun. 5, 3783.

Zheng, Y., Jiao, Y., Zhu, Y., Li, L.H., Han, Y., Chen, Y., Jaroniec, M., and Qiao, S.-Z. (2016). High electrocatalytic hydrogen evolution activity of an anomalous ruthenium catalyst. J. Am. Chem. Soc. 138, 16174–16181.

Supplemental Information

pH-Universal Water Splitting Catalyst:

Ru-Ni Nanosheet Assemblies

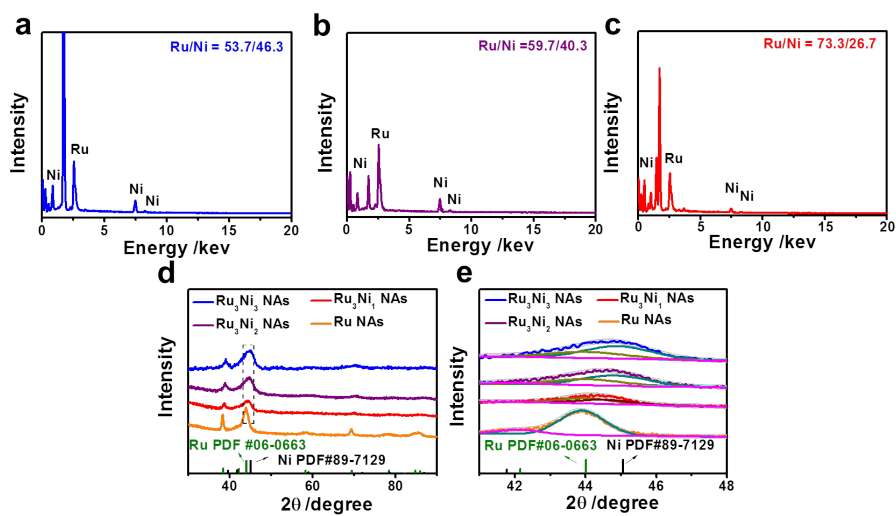Jian Yang, Qi Shao, Bolong Huang, Mingzi Sun, and Xiaoqing Huang

Figure S1. EDS spectra and XRD characterization of synthesized RuNi NAs, related to Figure 1.
(a-c) SEM-EDS spectra and (d) XRD patterns of Ru_3Ni_3 NAs, Ru_3Ni_2 NAs, Ru_3Ni_1 NAs and Ru NAs. (e) The main peak enlarged drawing corresponding to (d).
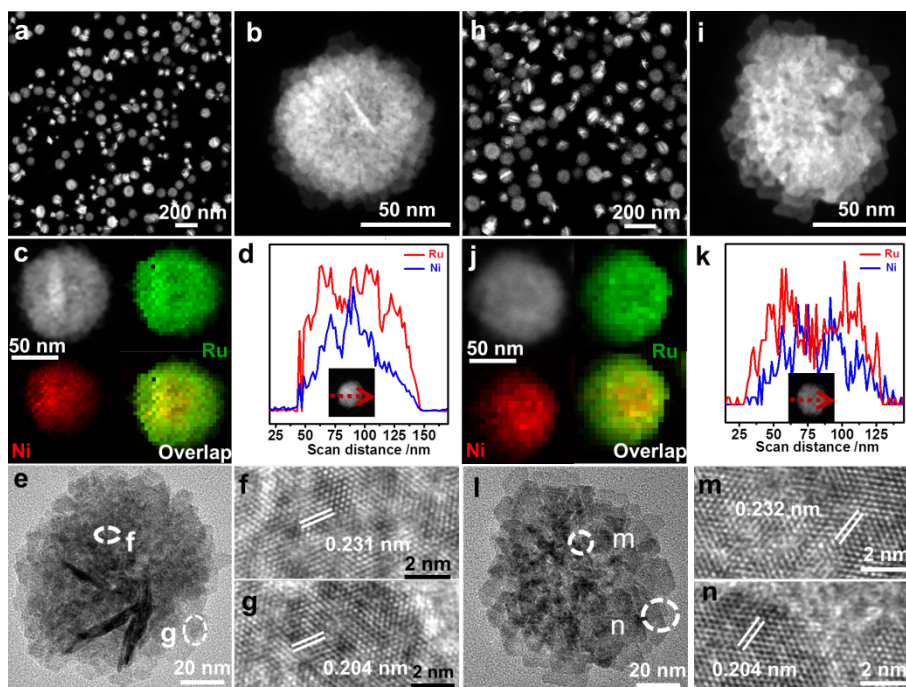
Figure S2. STEM, EDS and TEM images of synthesized RuNi NAs, related to Figure 1.

(a, b, h, i) HAADF-STEM images, (c, j) EDS elemental mapping images and (d, k) line scans of (a-d) Ru_3Ni_2 NA and (h-k) Ru_3Ni_1 NA. (e, l) TEM images and (f, g, m, n) HRTEM images of (e-g) Ru_3Ni_2 NA and (l-n) Ru_3Ni_1 NA.
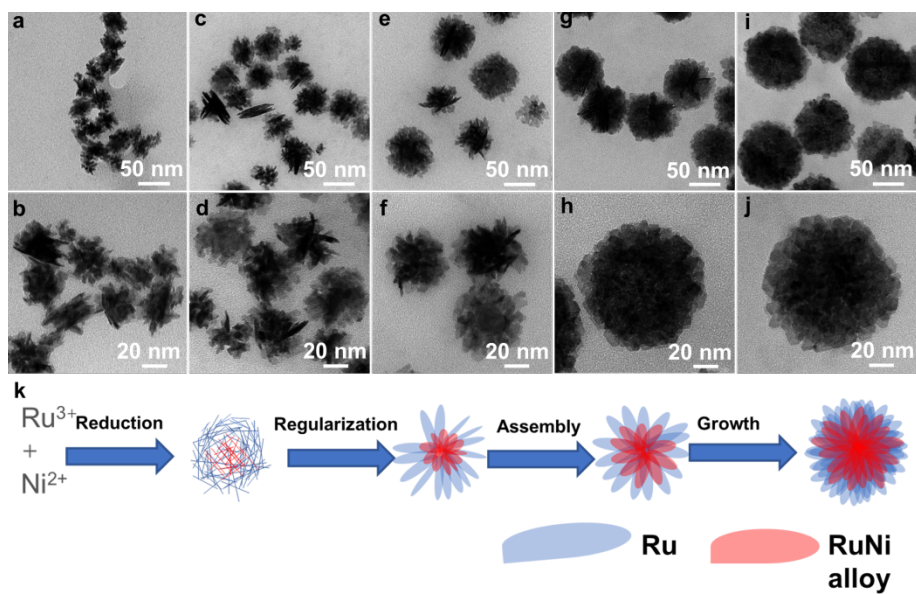
Figure S3. TEM images of the intermediates of the Ru$_3$Ni$_3$ NAs obtained at different reaction times, related to Figure 1.
(a, b) t = 25 min, (c, d) t = 40 min, (e, f) 1.5 h, (g, h) t = 3 h and (i, j) t = 5 h. (k) Schematic illustration on the growth of the Ru$_3$Ni$_3$ NAs.
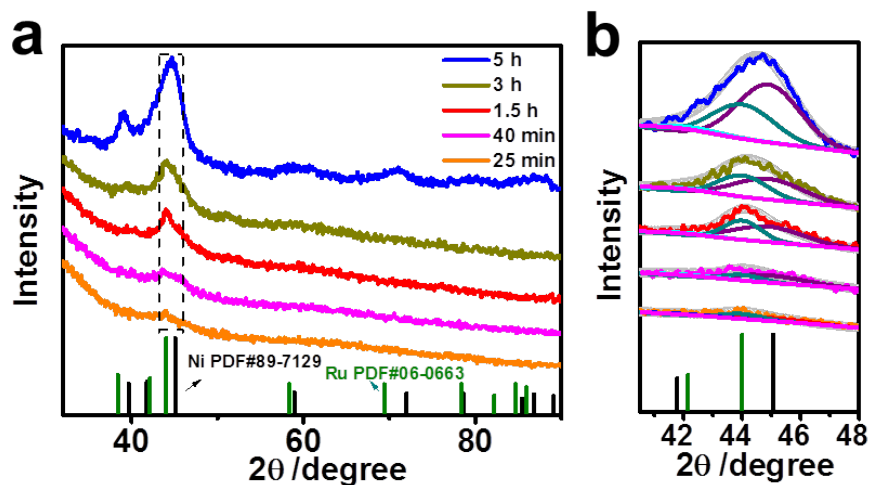
Figure S4. XRD characterization of the Ru$_3$Ni$_3$ NAs, related to Figure 1.
(a) XRD patterns of the intermediates of the Ru$_3$Ni$_3$ NAs obtained at different reaction time. (b) The main peak enlarged from the dashed region marked in (a).
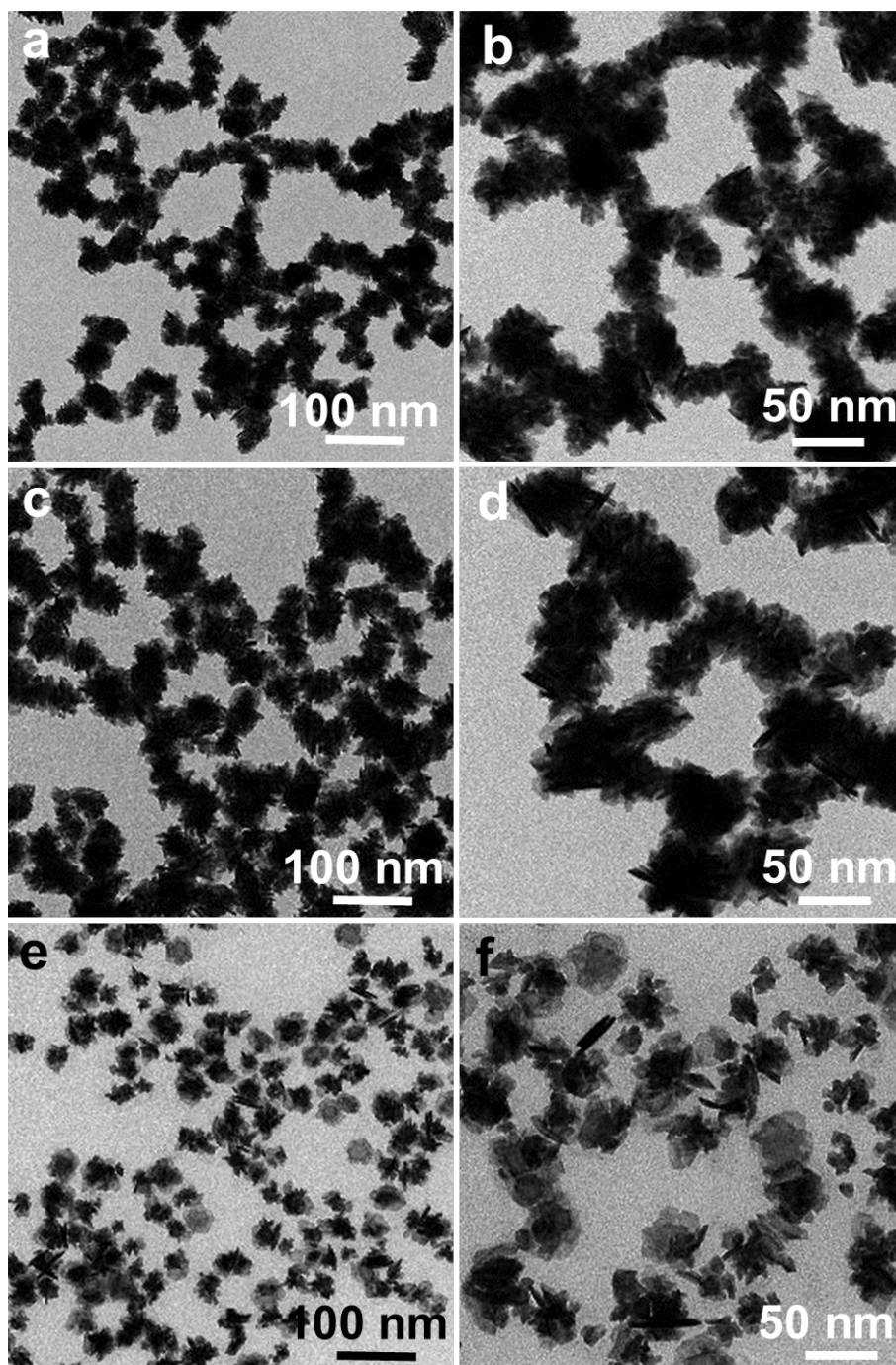
Figure S5. TEM images of the obtained products using the standard procedure for the Ru₃Ni₃ NAs except for using different amounts of phloroglucinol, related to Figure 1.
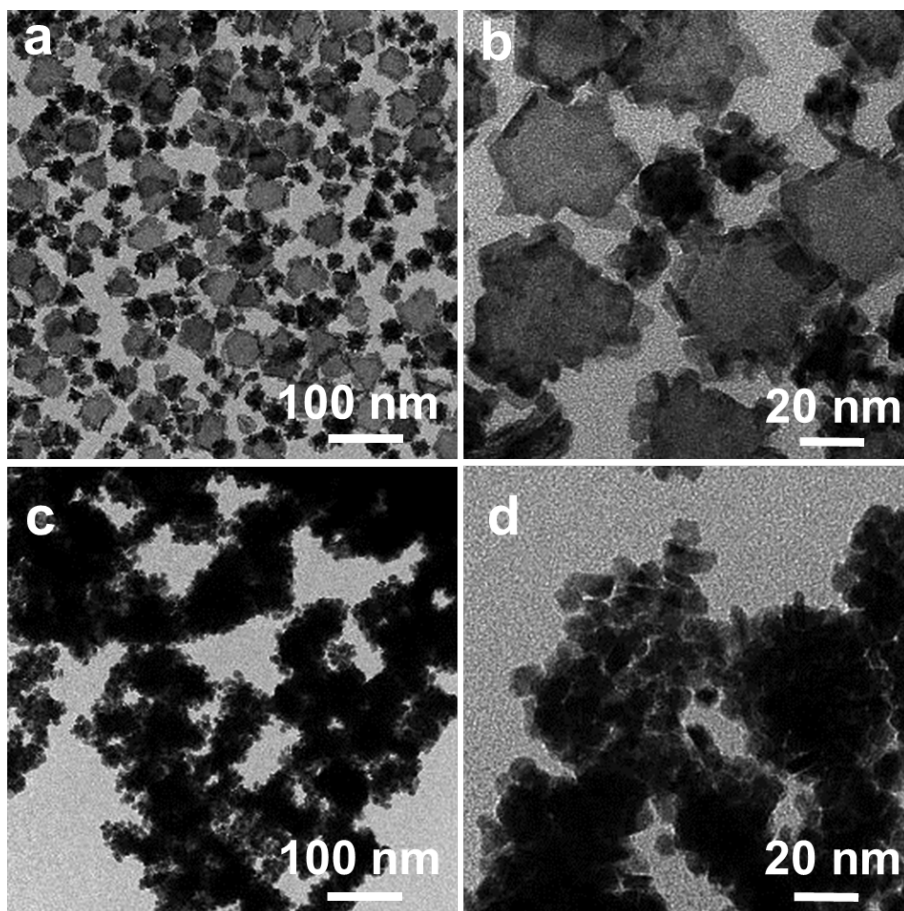
(a, b) 0 mg (c, d) 25.3 mg and (e, f) 100 mg.

Figure S6. TEM images of the obtained products using the standard procedure for the Ru$_3$Ni$_3$ NAs except for using different amounts of tetramethylammonium bromide, related to Figure 1.
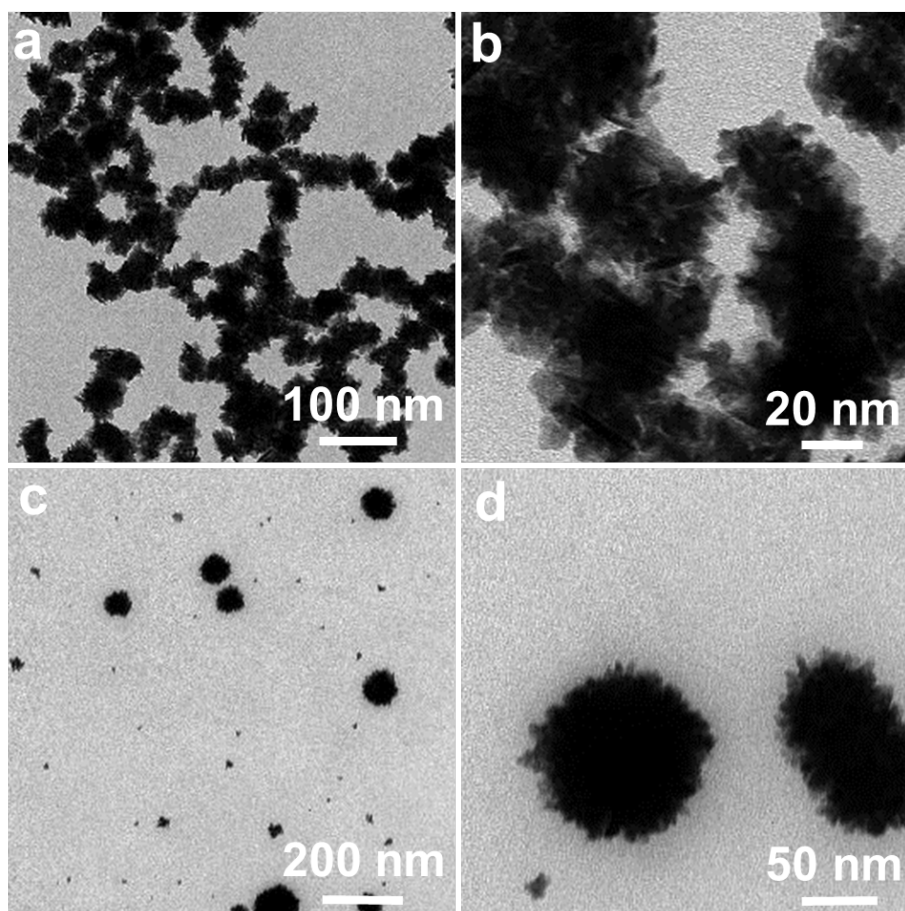
(a, b) 0 mg and (c, d) 20 mg.

Figure S7. TEM images of the obtained products using the standard procedure for the Ru₃Ni₃ NAs, related to Figure 1.

(a, b) without using PVP and (c, d) replacing benzyl alcohol with ethylene glycol.
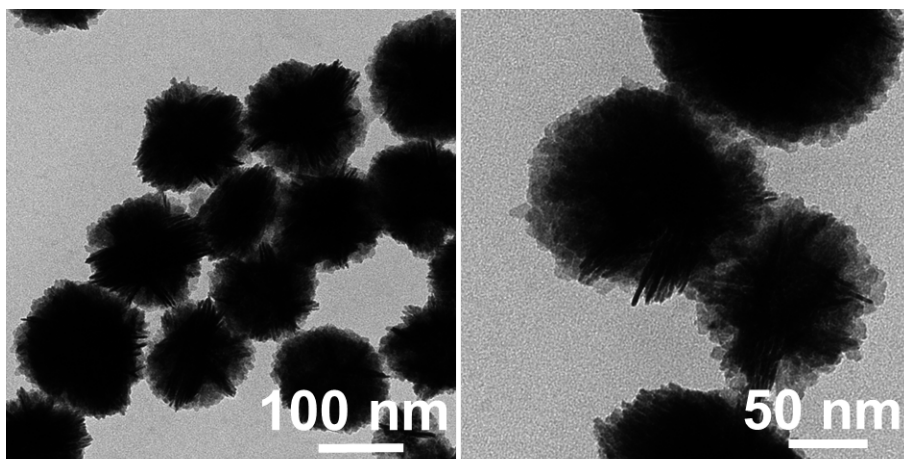
Figure S8. TEM images of Ru NAs using the standard procedure for the Ru$_3$Ni$_3$ NAs but without using Ni(acac)$_2$, related to Figure 1.
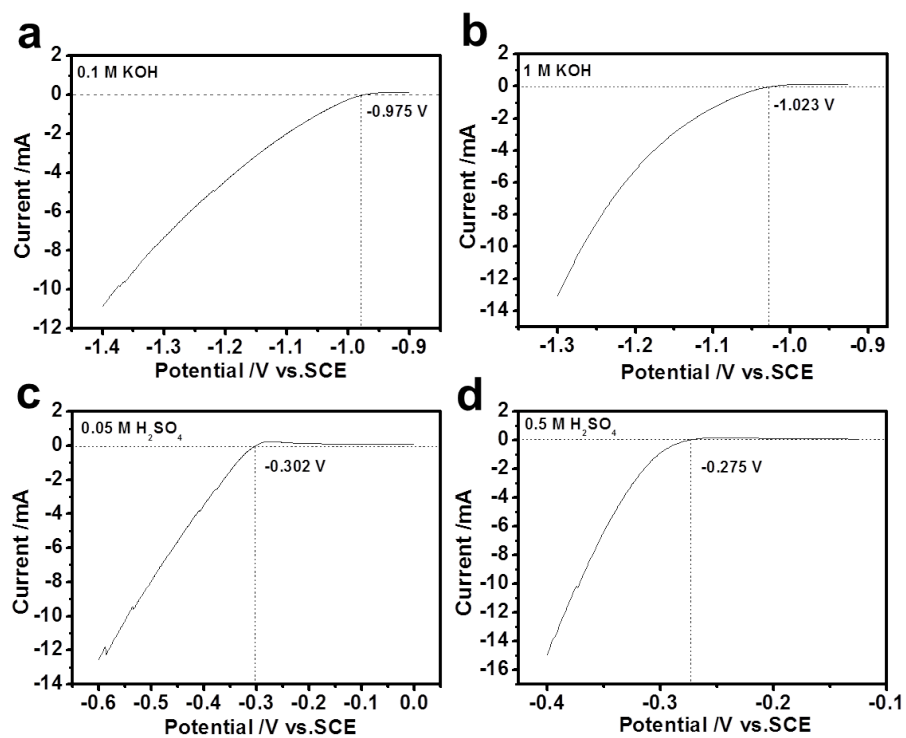
Figure S9. Calibration of the saturated calomel electrode (SCE) electrode with respect to RHE in different electrolytes. Scan rate: 1 mV s^{-1}, related to Figure 2.
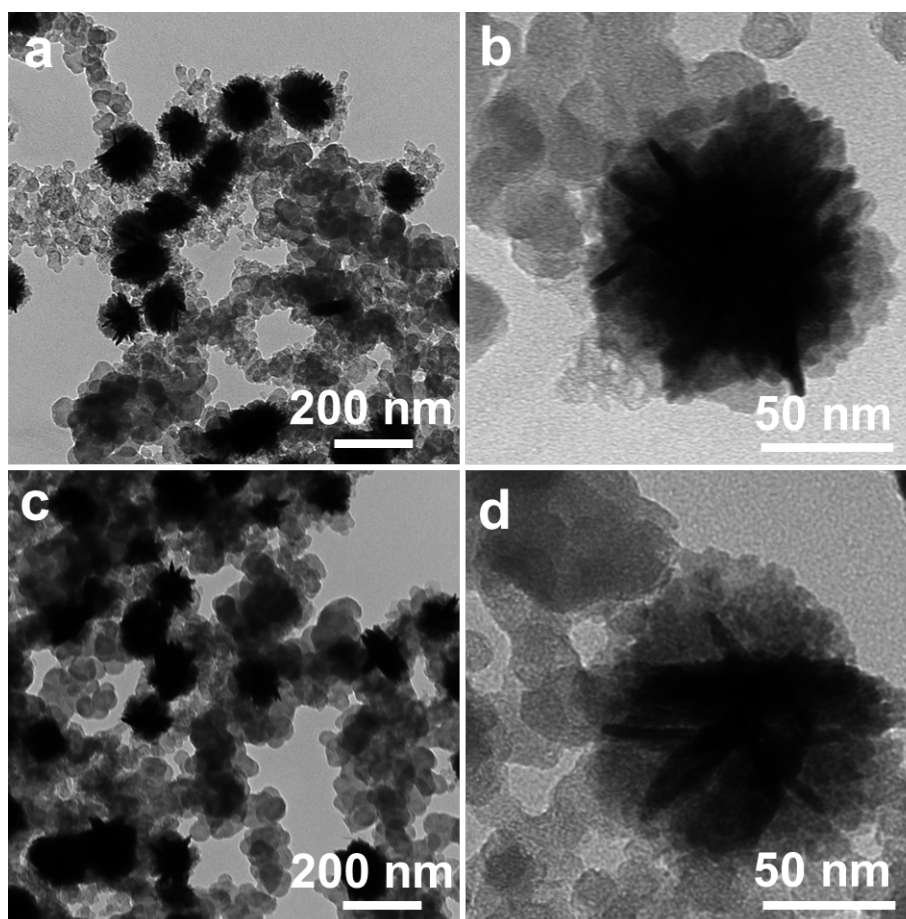
Figure S10. TEM images of Ru$_3$Ni$_3$ NAs loaded on the carbon powder after heat treatment in air at (a, b) 250 °C for 1 h and (c, d) 350 °C for 2 h, related to Figure 2.
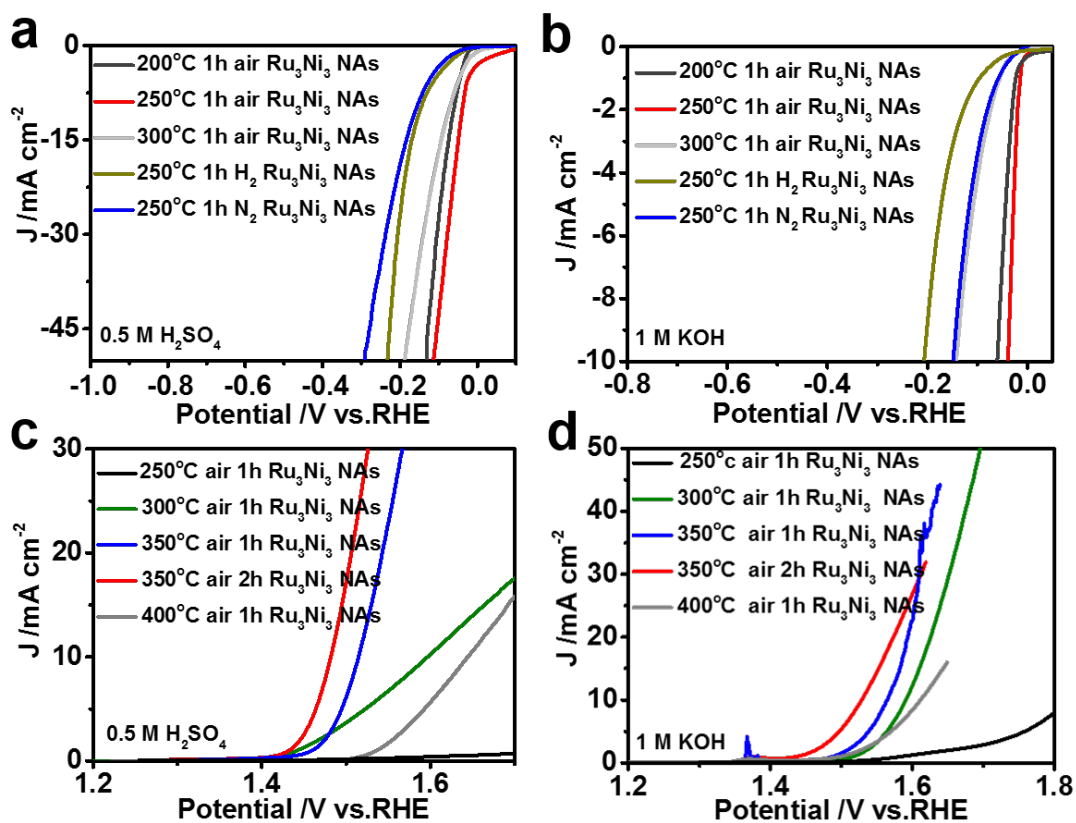
Figure S11. HER and OER performances of Ru₃Ni₃ NAs in different environment, related to Figure 2.

HER performances of Ru₃Ni₃ NAs in (a) 0.5 M H₂SO₄ and (b) 1 M KOH through heat treatment at different conditions. OER performances of Ru₃Ni₃ NAs in (c) 0.5 M H₂SO₄ and (d) 1 M KOH after heat treatment under different conditions.
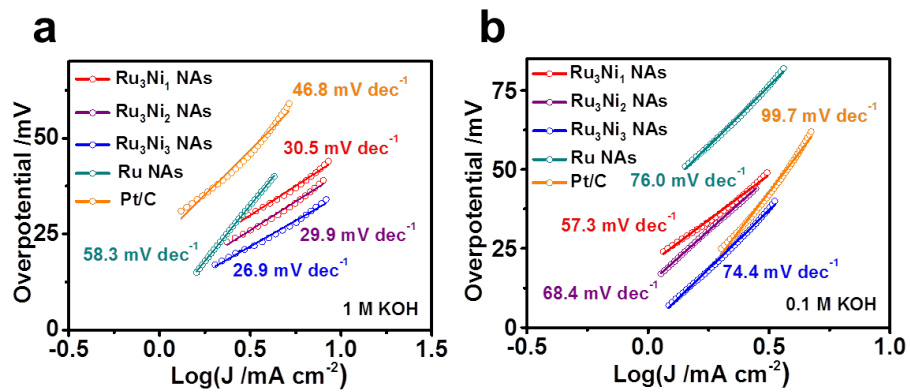
Figure S12. The corresponding HER Tafel plots of Ru$_3$Ni$_3$ NAs, Ru$_3$Ni$_2$ NAs, Ru$_3$Ni$_1$ NAs, Ru NAs and Pt/C in different environment, related to Figure 2.

(a) 1 M KOH and (b) 0.1 M KOH derived from Figure 2a, b.
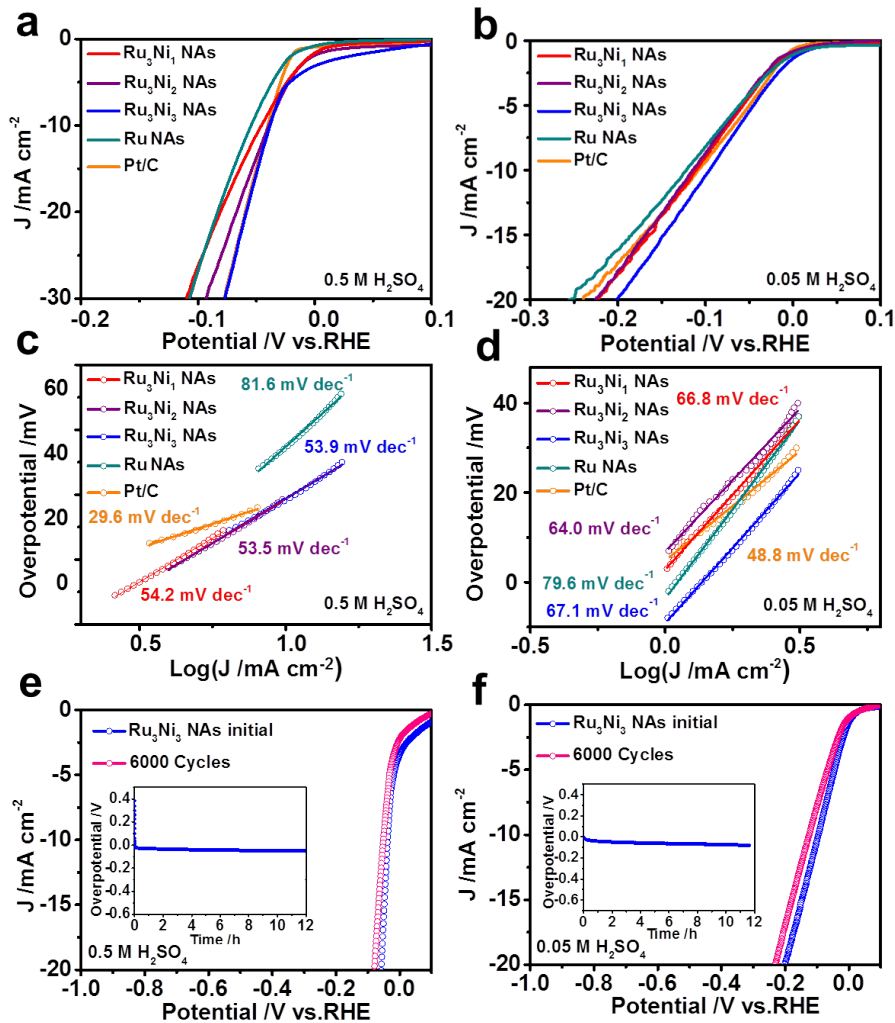
Figure S13. HER performances of Ru₃Ni₃ NAs, Ru₃Ni₂ NAs, Ru₃Ni₁ NAs, Ru NAs and Pt/C in acidic condition, related to Figure 2.
(a) The polarization curves and (c) the corresponding Tafel plots in 0.5 M H_2SO_4. (b) The polarization curves and (d) the corresponding Tafel plots in 0.05 M H_2SO_4. Scan rates are 5 mV s⁻¹. Polarization curves of Ru₃Ni₃ NAs before and after 6000 cycles in (e) 0.5 M H_2SO_4 and (f) 0.05 M H_2SO_4 at a scan rate of 5 mV s⁻¹. Inset: Chronopotentiometry curves of Ru₃Ni₃ NAs in (e) 0.5 M H_2SO_4 and (f) 0.05 M H_2SO_4 solutions at current density of 5 mA cm⁻².
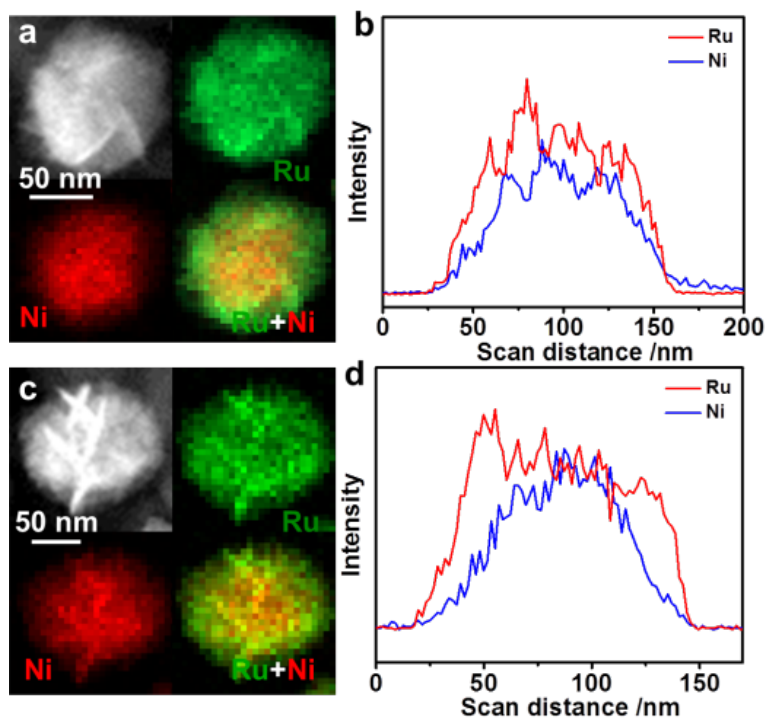
Figure S14. STEM image and elemental mapping of Ru$_3$Ni$_3$ NAs loaded on the carbon powder after heat treatment in air at different temperature and time, related to Figure 3.

(a) 250 °C for 1 h and (c) 350 °C for 2 h. Line scans of Ru$_3$Ni$_3$ NAs after heat treatment in air at (b) 250 °C for 1 h and (d) 350 °C for 2 h.
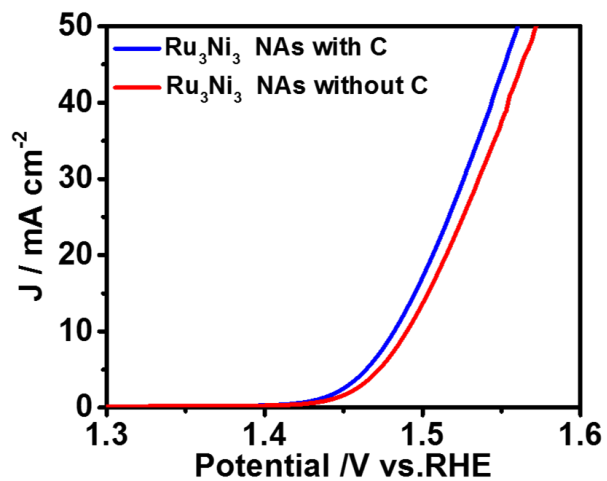
Figure S15. OER performances of Ru₃Ni₃ NAs with C and without C in the 0.5 M H_2SO_4, related to Figure 3.
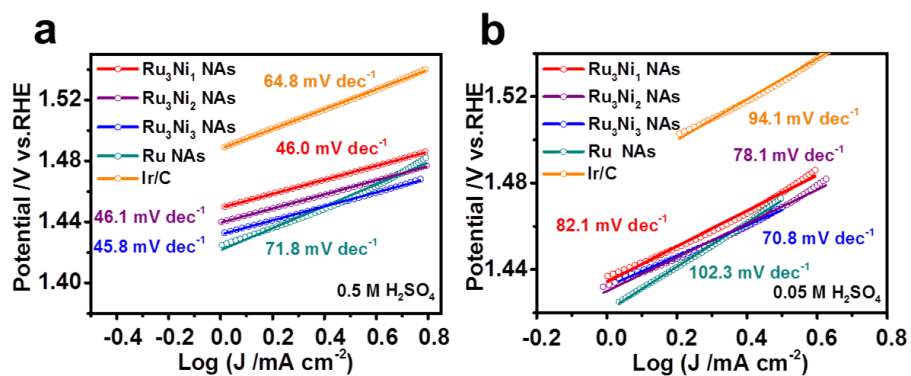
Figure S16. The corresponding OER Tafel plots of Ru₃Ni₃ NAs, Ru₃Ni₂ NAs, Ru₃Ni₁ NAs, Ru NAs and Ir/C in different acid environment, related to Figure 3.
(a) 0.5 M H_2SO_4 and (b) 0.05 M H_2SO_4 derived from Figure 3a, b.
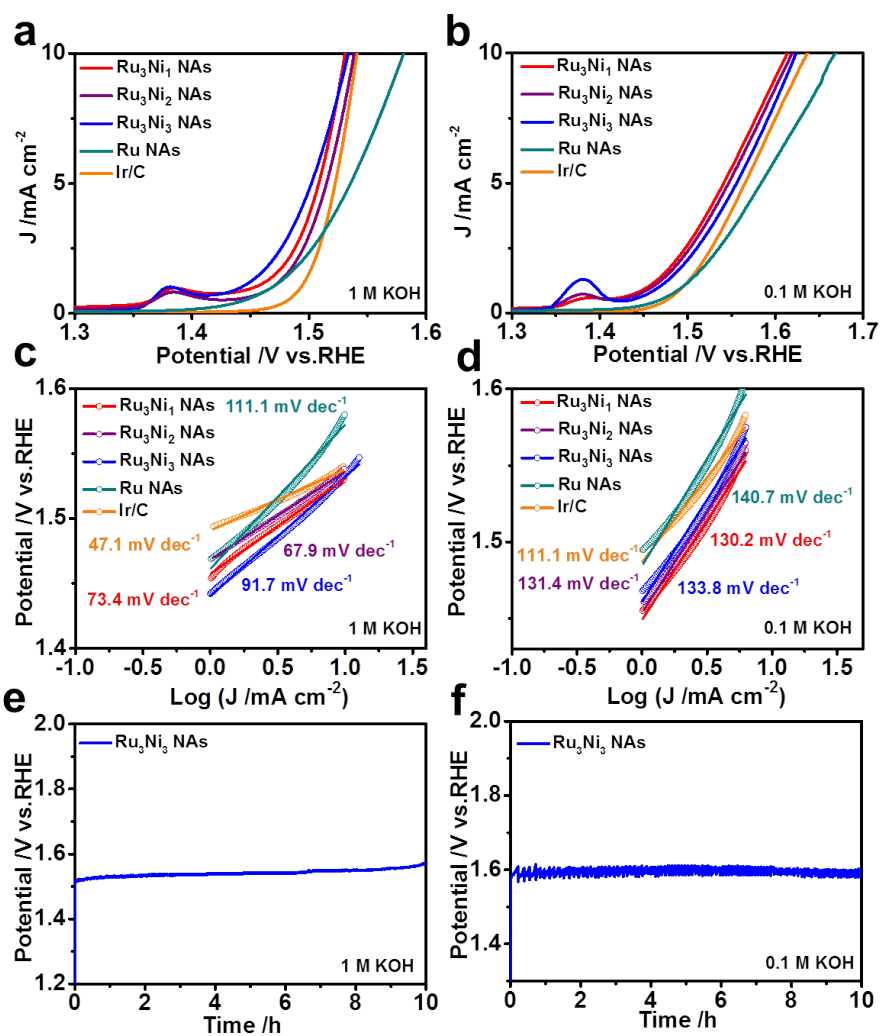
Figure S17. OER performances of Ru₃Ni₃ NAs, Ru₃Ni₂ NAs, Ru₃Ni₁ NAs, Ru NAs and Ir/C in alkaline condition, related to Figure 3.
(a) The polarization curves and (c) the corresponding Tafel plots in 1 M KOH. (b) The polarization curves and (d) the corresponding Tafel plots in 0.1 M KOH. Scan rates are 5 mV s^{-1}. Chronopotentiometry curves of Ru₃Ni₃ NAs in (e) 1 M KOH and (f) 0.1 M KOH solutions at current density of 5 mA cm^{-2}.
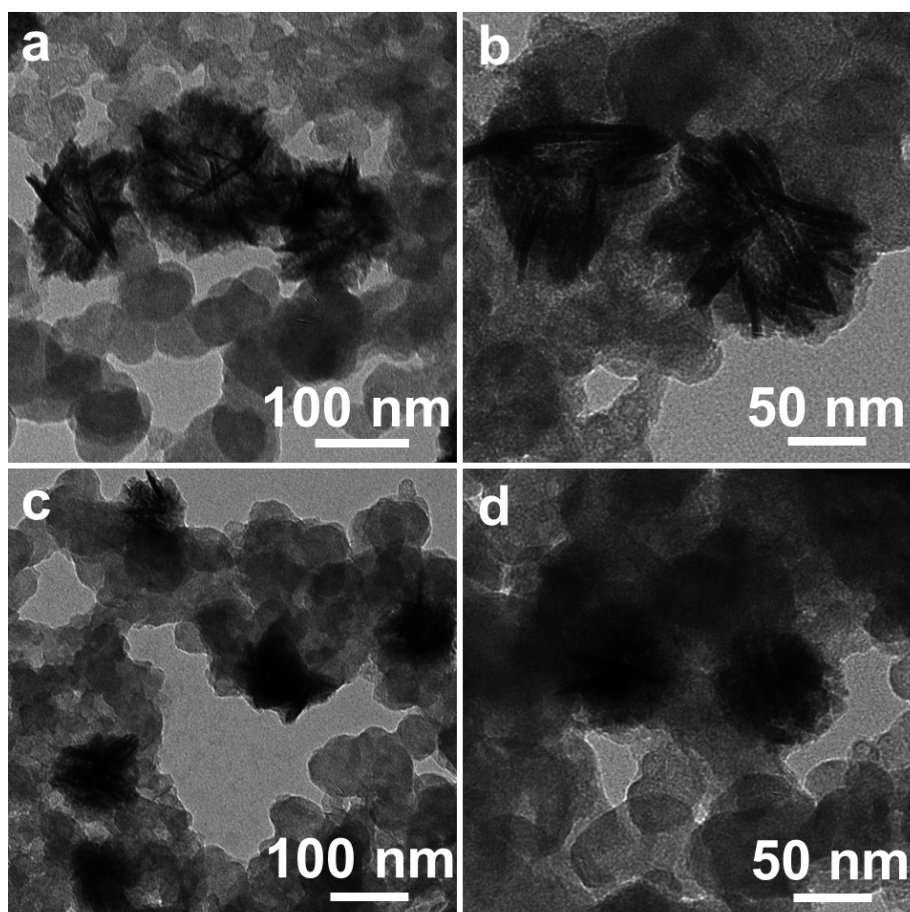
Figure S18. TEM images of Ru₃Ni₃ NAs after the OER stability tests, related to Figure 3.

(a-b) 0.5 M H_2SO_4 and (c-d) 1 M KOH.
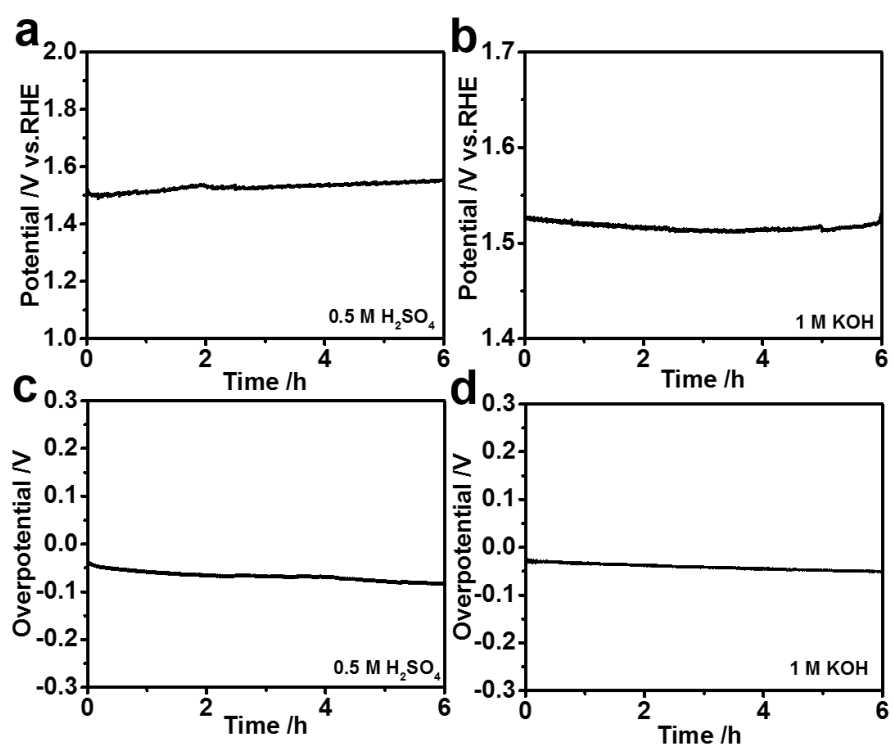
Figure S19. Chronopotentiometry curves of Ru$_3$Ni$_3$ NAs, related to Figure 3.

(a) 0.5 M H$_2$SO$_4$ and (b) 1 M KOH for OER and in (c) 0.5 M H$_2$SO$_4$ and (d) 1 M KOH for HER.
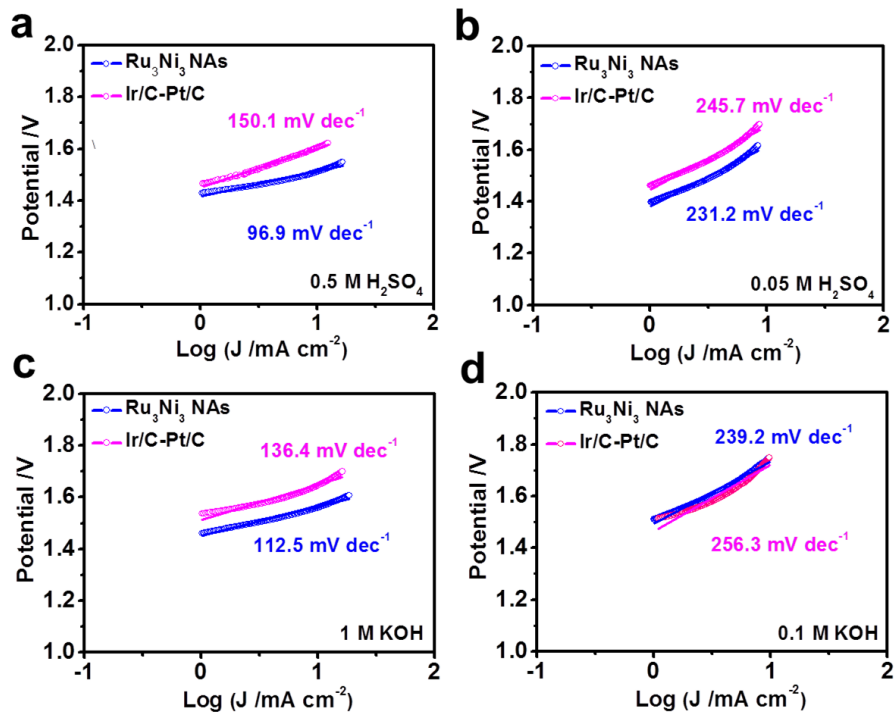
Figure S20. The corresponding water splitting Tafel plots of Ru₃Ni₃ NAs and Ir/C-Pt/C, related to Figure 4.
(a) 0.5 M H$_2$SO$_4$, (b) 0.05 M H$_2$SO$_4$, (c) 1 M KOH and (d) 0.1 M KOH, derived from Figure 4a.
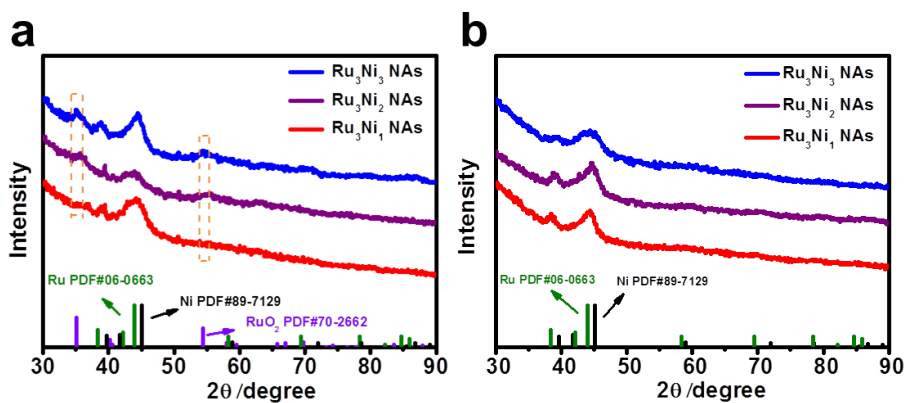
Figure S21. The XRD patterns of Ru$_3$Ni$_3$ NAs, Ru$_3$Ni$_2$ NAs and Ru$_3$Ni$_1$ NAs after heat treatment in air at different temperature and time, related to Figure 5.

(a) 350 °C for 2 h and (b) 250 °C for 1 h.
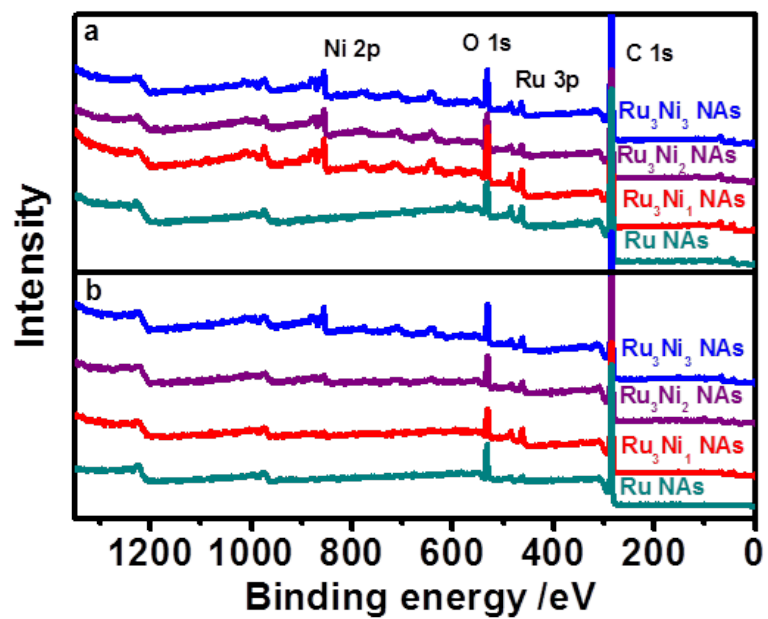
Figure S22. Full scan XPS curves of Ru$_3$Ni$_3$ NAs, Ru$_3$Ni$_2$ NAs, Ru$_3$Ni$_1$ NAs and Ru NAs treated in different environment, related to Figure 5.
(a) at 350 °C in air for 2h and (b) at 250 °C in air for 1h.
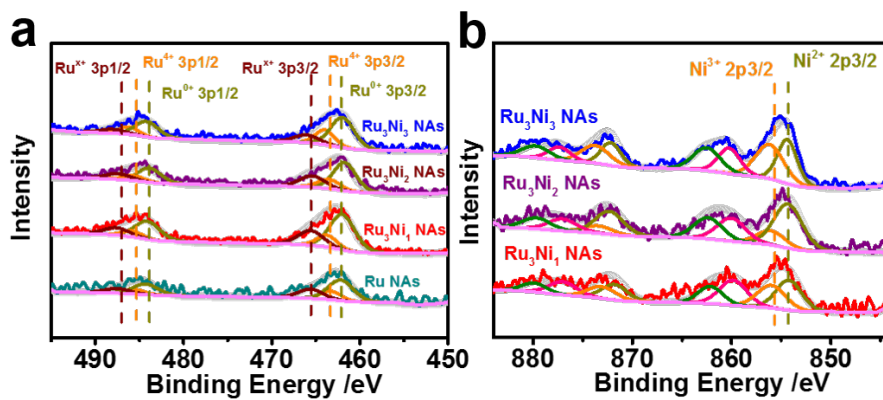
Figure S23. XPS analysis, related to Figure 5.

(a) Ru 3p and (b) Ni 2p curves of Ru$_3$Ni$_3$ NAs, Ru$_3$Ni$_2$ NAs, Ru$_3$Ni$_1$ NAs and Ru NAs treated heated at 250 °C in air for 1h.
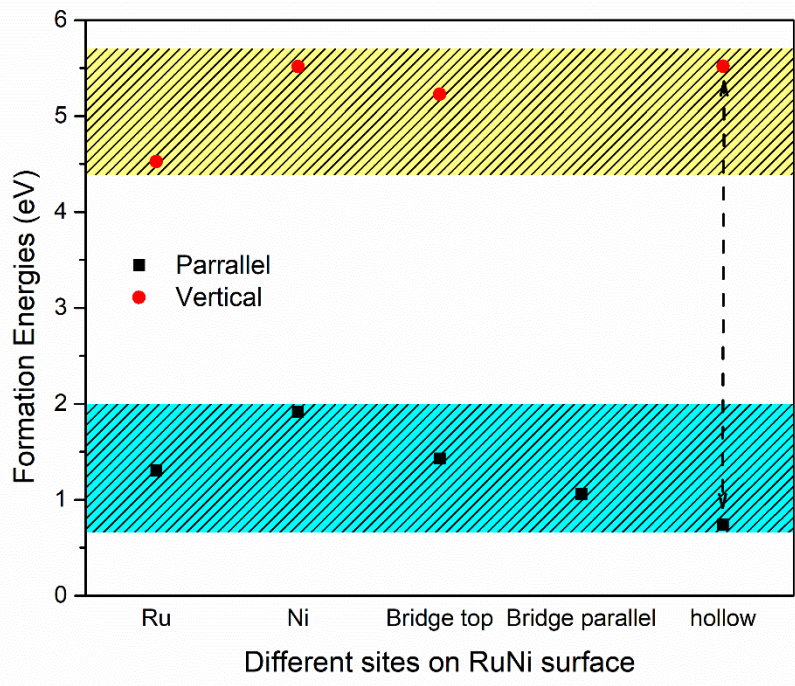
Figure S24. Diagram of absorption energies of absorbed oxygen on RuNi (0001) surface at different sites, related to Figure 6.
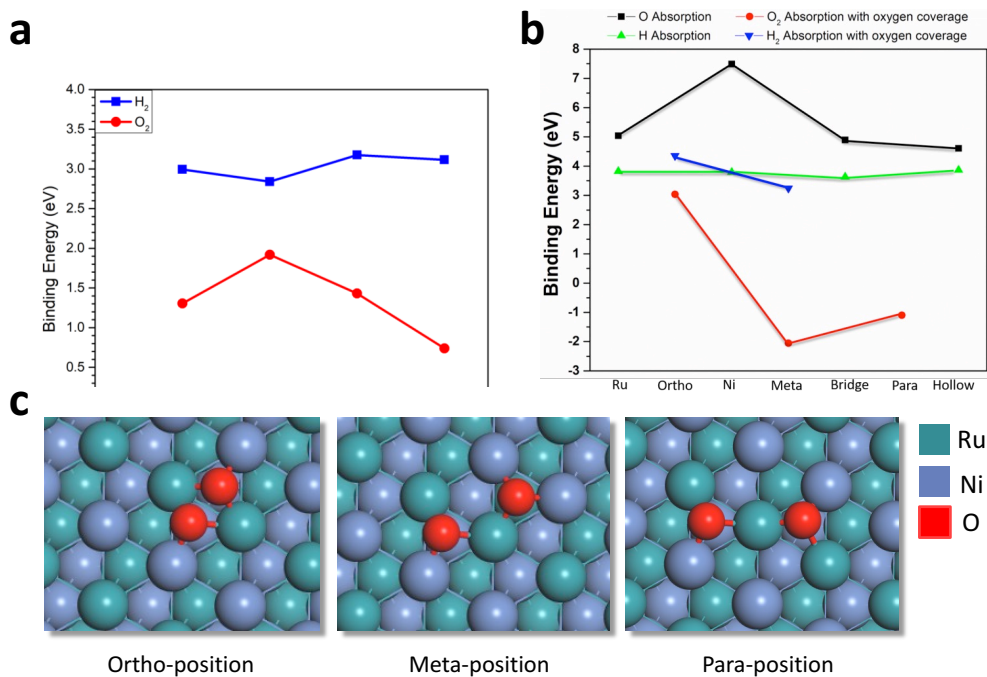
Figure S25. The binding energies diagrams and structural configurations, related to Figure 6.

(a) pristine surface, (b) different partial O-coverage are illustrated, focusing on the cubic phase RuNi (111) surface with considerations on the absorptions of O, H, O_2 and H_2, respectively. (c) Structure configuration of oxygen adsorption.
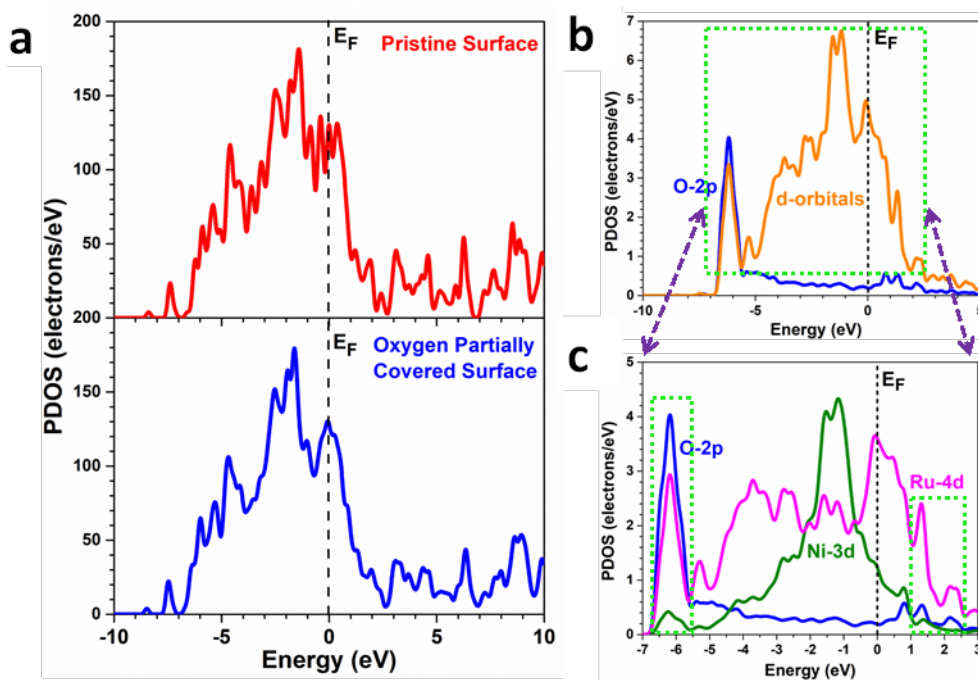
Figure S26. The Comparison of DOS between pristine and oxygen partially covered RuNi surface, related to Figure 6.

(a) Comparison of TDOS between pristine surface and oxygen covered surface. (b) The PDOS of p orbitals from oxygen cover and d orbitals from top surface layer of RuNi model. (c) Illustration of the orbital overlap among O-2p orbitals, Ni-3d orbitals and Ru-4d orbitals.
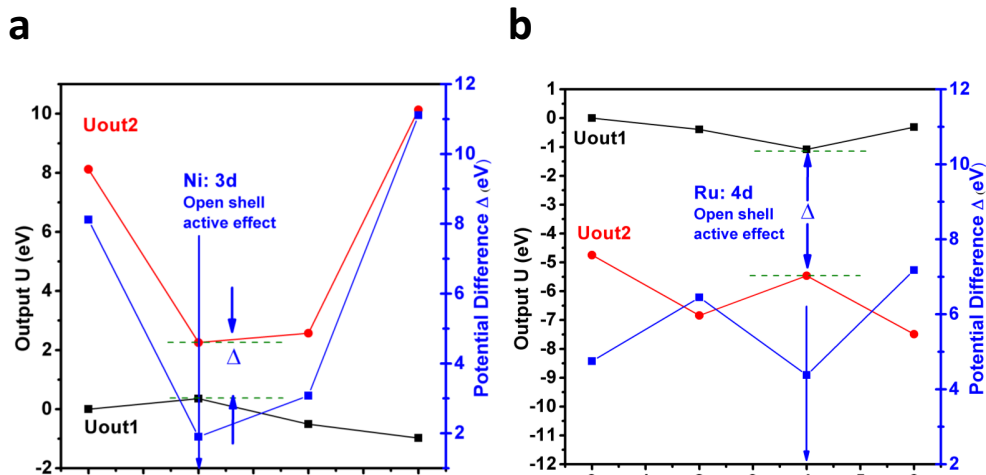
Figure S27. The on-site orbital potential energy projections (Uout1 and Uout2) related to Figure 6.

(a) Ni-3d and (b) Ru-4d on the partially O-covered RuNi surface are demonstrated.
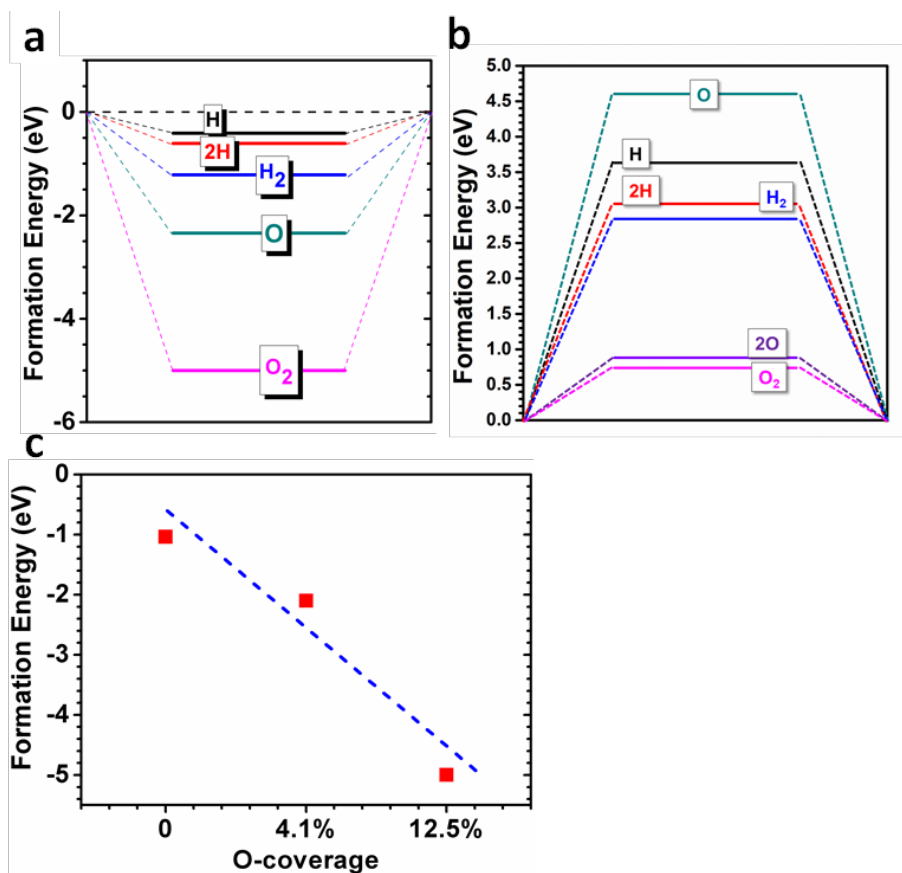
Figure S28. Formation energy of HER and OER, related to Figure 6.

(a) The formation energy for the HER and OER in hexagonal RuNi surface system with partial oxidation states. (b) The chemisorption energy for the HER and OER in cubic phase of RuNi surface system. (c) The O_2 formation energy comparison with different O-coverage on the hexagonal RuNi surface system

Table S1. Summary of activities of HER and OER of Ru-Ni NAs, Ru NAs, Pt/C, Ir/C in alkaline and acidic electrolytes, related to Figure 2 and Figure 3.

			Ru$_3$Ni$_3$ NAs	Ru$_3$Ni$_2$ NAs	Ru$_3$Ni$_1$ NAs	Ru NAs	Pt/C	Ir/C
1 M KOH	Overpotential (mV)	**HER**	39	42	44	62	90	—
		OER	304	309	301	351	—	311
	Tafel slope (mV dec^{-1})	**HER**	26.9	29.9	30.5	58.3	46.8	—
		OER	91.7	67.9	73.4	111.1	—	47.1
0.1 M KOH	Overpotential (mV)	**HER**	119	127	123	152	132	—
		OER	394	390	384	439	—	407
	Tafel slope (mV dec^{-1})	**HER**	74.4	68.4	57.3	76.0	99.7	—
		OER	133.8	131.4	130.2	140.7	—	111.1
0.5 M H$_2$SO$_4$	Overpotential (mV)	**HER**	39	39	46	55	41	—
		OER	252	260	268	277	—	328
	Tafel slope (mV dec^{-1})	**HER**	53.9	53.5	54.2	81.6	29.6	—
		OER	45.8	46.1	46.0	71.8	—	64.8
0.05 M H$_2$SO$_4$	Overpotential (mV)	**HER**	96	115	112	122	109	—
		OER	312	313	327	341	—	372
	Tafel slope (mV dec^{-1})	**HER**	67.1	64.0	66.8	79.6	48.8	—
		OER	70.8	78.1	82.1	102.3	—	94.1

Table S2. Summary of the recently reported HER electrocatalysts in alkaline and acidic electrolytes. [a]without *i*R compensation. η denotes overpotential, related to Figure 2.

Catalyst	Electrolyte	Current Density	η /mV	Tafel slope (mV/dec)	Ref.
[a]Ru_3Ni_3 NAs	1 M KOH 0.1 M KOH 0.5 M H_2SO_4 0.05 M H_2SO_4	10 mA cm^{-2}	39 119 39 96	26.9 74.4 53.9 67.1	**This work**
[a]A-Ni-C	0.5 M H_2SO_4	10 mA cm^{-2}	34	41	*Nat. Commun.* **7**, 10667 (2016).
[a]MoSx/NCNT	0.5 M H_2SO_4	10 mA cm^{-2}	110	*40*	*Nano Lett.* **14**, 1228-1233 (2014).
Ru@C_2N	0.5 M H_2SO_4	10 mA cm^{-2}	22	30	*Nat. Nanotechnol.* **12**, 441-446 (2017).
SV-MoS_2	0.5 M H_2SO_4	10 mA cm^{-2}	170	60	*Nat. Mater.* **15**, 48-53 (2016).
FeP NA/Ti	0.5 M H_2SO_4	10 mA cm^{-2}	55	38	*Angew. Chem. Int. Ed.* **53**, 12855-12859 (2014).
CoMoSx	0.1 M $HClO_4$ 0.1 M KOH	5 mA cm^{-2}	207 158	/	*Nat. Mater.* **15**, 197-203 (2016).
NiFeOx/CFP	1 M KOH	10 mA cm^{-2}	88	84.6	*Nat. Commun.* **6**, 7261 (2015).
MoCx nanooctahedrons	1 M KOH	10 mA cm^{-2}	151	59	*Nat. Commun.* **6**, 6512 (2015).
CoNx/C	1 M KOH	10 mA cm^{-2}	170	75	*Nat. Commun.* **6**, 7992 (2015).
WC/Ni foam	0.1 M KOH	10 mA cm^{-2}	220	/	*J. Am. Chem. Soc.* **137**, 5480-5485 (2015).
CoFeP	1 M KOH	10 mA cm^{-2}	79	40	*Energy Environ. Sci.* **9**, 2257-2261 (2016).
$Ni(OH)_2$/Pt-islands/Pt(111)	0.1 M KOH	10 mA cm^{-2}	130	/	*Science 334, 1256 (2011)*
β-$Ni(OH)_2$/Pt	1 M KOH	10 mA cm-2	115	42	*ACS Energy Lett. 3, 237 (2018).*

Table S3. Summary of the recently reported OER electrocatalysts in alkaline and acidic electrolytes. [a]without *i*R compensation. η denotes overpotential, related to Figure 3.

Catalyst	Electrolyte	Current Density	η /mV	Tafel slope (mV/dec)	Ref.
[a]Ru_3Ni_3 NAs	0.5 M H_2SO_4 0.05 M H_2SO_4 1 M KOH 0.1 M KOH	10 mA cm^{-2}	252 312 304 394	45.8 70.8 91.7 133.8	This work
$IrO_x/SrIrO_3$	0.5 M H_2SO_4	10 mA cm^{-2}	270	/	*Science* **353**, 1011-1014 (2016).
$IrNiO_x$/Meso-ATO	0.05 M H_2SO_4	10 mA cm^{-2}	320	/	*Angew. Chem. Int. Ed.* **54**, 2975-2979 (2015).
Ir	1 M H_2SO_4 1 M KOH	10 mA cm^{-2}	360 430	/	*J. Am. Chem. Soc.* **137**, 4347-4357 (2015).
Ru	1 M H_2SO_4 1 M KOH	10 mA cm^{-2}	340 320	/	*J. Am. Chem. Soc.* **135**, 16977-16987 (2013).
N-doped GM	0.1 M KOH	10 mA cm^{-2}	540	/	*Adv. Mater.* **28**, 6845-6851 (2016).
S, S-CNT	1 M KOH	10 mA cm^{-2}	350	95	*Adv. Energy Mater.* **6**, 1501966 (2016).
N/Co-doped PCPRGO	0.1 M KOH	10 mA cm^{-2}	430	292	*Adv. Funct. Mater.* **25**, 872-882 (2015).

Table S4. The area ratios of Ru^{x+}, Ru^{4+} and Ru^0 in Ru_3Ni_3 NAs, Ru_3Ni_2 NAs, Ru_3Ni_1 NAs and Ru NAs after thermal treatment in air at 350 °C for 2h, derived from Ru 3p XPS results, related to Figure 5.

Area ratios	Ru^{x+} %	Ru^{4+} %	Ru^0 %	Total %
Ru_3Ni_3 NAs	25.59	57.00	17.41	100
Ru_3Ni_2 NAs	29.32	44.46	26.22	100
Ru_3Ni_1 NAs	26.84	44.57	28.59	100
Ru NAs	24.08	29.89	46.03	100

Table S5. The area ratios of Ru^{x+}, Ru^{4+} and Ru^0 in Ru_3Ni_3 NAs, Ru_3Ni_2 NAs, Ru_3Ni_1 NAs and Ru NAs after thermal treatment in air at 250 °C for 1h, derived from Ru 3p XPS results, related to Figure 5.

Area ratios	Ru^{x+} %	Ru^{4+} %	Ru^0 %	Total %
Ru_3Ni_3 NAs	16.31	23.95	59.74	100
Ru_3Ni_2 NAs	25.15	18.08	56.77	100
Ru_3Ni_1 NAs	25.58	16.36	58.06	100
Ru NAs	25.21	18.71	56.08	100

Table S6. Absorption energy of different sites on RuNi (0001) surface, related to Figure 6.

Site	Oxygen Position	Formation Energies (eV)	Oxygen Dissociation
Ni Top	parallel	1.918	Yes
	vertical	5.514	No
Ru Top	parallel	1.305	Yes
	vertical	4.526	No
Hollow	parallel	0.739	Yes
	vertical	5.519	No
Bridge top	parallel	1.430	Yes
	vertical	5.227	No
Bridge parallel	parallel	1.057	Yes

-

Table S7. Formation energy of Ru top site on distorted RuNi (0001) surface, , related to Figure 6.

Site	Position	Formation energies (eV)	Oxygen Dissociation
Ru Top	parallel	4.485	No
	vertical	4.811	No

TRANSPARENT METHODS

Materials

Ruthenium (III) acetylacetonate (Ru(acac)$_3$, 97%) was purchased from Sigma-Aldrich. Nickel (II) acetylacetonate (Ni(acac)$_2$, 96%) and polyvinylpyrrolidone (PVP, MW=58000) were provided by J&K Scientific LTD. Benzyl alcohol (C$_7$H$_8$O, 99%) was purchased from Sinopharm Chemical Reagent Co. Ltd. (Shanghai, China). Phloroglucinol (C$_6$H$_6$O$_3$, 99%) and ethylene glycol (C$_2$H$_7$O, 99%) were purchased from Aladdin. All chemicals were used without further purification. The water (18 MΩ cm^{-1}) used in all the experiments was prepared by passing through an ultra-pure purification system (Aqua Solutions).

Preparation of hierarchical Ru-Ni NAs.

In a typical preparation of Ru$_3$Ni$_3$ NAs, 10 mg Ru(acac)$_3$, 6.3 mg Ni(acac)$_2$, 75.9 mg phloroglucinol, 5 mg tetramethylammonium bromide, 100 mg PVP and 10 mL benzyl alcohol were added into a 35 mL glass vial. After the vial was capped, the mixture was ultrasonicated for approximately 40 min. The resulting homogeneous mixture was then heated from room temperature to 160 °C and maintained at 160 °C for 5 h in an oil bath. The products were then collected by centrifugation and washed with an ethanol/acetone mixture. The preparations of the Ru$_3$Ni$_2$ NAs and Ru$_3$Ni$_1$ NAs were achieved by changing the amounts of Ni(acac)$_2$ from 6.3 mg to 4.2 mg and 2.1 mg while keeping the other parameters constant. The Ru NAs was prepared using the same procedure without Ni(acac)$_2$.

Characterizations

The samples were prepared by dropping ethanol dispersions of the samples on carbon-coated copper TEM grids using pipettes and drying them under ambient conditions. Low-magnification transmission electron microscopy (TEM)

was conducted on a HITACHI HT7700 transmission electron microscope applying an acceleration voltage of 120 kV. High-magnification TEM and HAADF-STEM images were conducted on an FEI Tecnai F20 transmission electron microscope with an acceleration voltage of 200 kV. Powder X-ray diffraction (PXRD) patterns were collected by an X'Pert-Pro MPD diffractometer (Netherlands PANalytical) with a Cu Kα X-ray source (λ=1.540598 Å). X-ray photoelectron spectra (XPS) were collected with an SSI S-Probe XPS spectrometer. All spectra used for the calculation of the d-band centre were corrected by a Shirley background. The d-band centres of the different catalysts were obtained by using the equation: $\frac{\int N(\varepsilon)\varepsilon d\varepsilon}{\int N(\varepsilon)d\varepsilon}$ in the range from 0 eV to -9.0 eV. N represents the density of states.

Electrochemical measurements.

A three-electrode system controlled by a CHI 660E electrochemistry workstation was used to carry out the electrochemical measurements. All Ru-Ni NAs with different ratios were loaded on the carbon powder (20% loading). The catalyst (2 mg) was mixed with isopropanol (1 mL) and Nafion (5 μL). A homogeneous ink was obtained after sonication (30 min). The working electrode (diameter: 0.5 cm, area: 0.196 cm^{-2}) was fabricated by casting 10 μL of the catalyst ink onto a glassy-carbon electrode (GCE). The reference electrode was a saturated calomel electrode (SCE). The counter electrode was a carbon rod. No iR compensation was provided through positive feedback using the CHI 660E electrochemistry workstation. Linear sweep voltammetry (LSV) was carried out with a scan rate of 5 mV s^{-1}. The working electrode was held at a constant current density of 5 mA cm^{-2} and 10 mA cm^{-2} for a continuous time, and the operating potential was finally measured as a function of time.

DFT models and calculations.

We used the CASTEP code to perform our DFT+U calculations (Clark et al., 2005). In this framework, we use the rotationally invariant (Anisimov type) DFT+U functional (Vladimir et al., 1997) and the Hubbard U parameter self-consistently determined for the pseudized Ni-3d and Ru-4d orbital by our new linear response method (Huang, 2016), which have been already successfully reflecting the electron-electron Coulomb potential for the semi-core orbitals should be considered when using DFT+U (Huang, 2016; Huang et al. 2016; Huang 2014; Huang, 2016; Huang, 2016). The geometry optimization used the Broyden-Fletcher-Goldfarb-Shannon (BFGS) algorithm through all calculations.

The PBE functional was chosen for PBE+U calculations with cutoff energy of 750 eV, with the valence electron states expressed in a plane-wave basis set. The ensemble DFT (EDFT) method of Marzari et al. (Marzari et al., 1997) is used for convergence. The supercell of buckle hexagonal Ru-Ni surface model was chosen with sizes of 108 atoms (i.e. $Ru_{54}Ni_{54}$) and 6-layer thick. The vacuum thickness is set to be 15 Å. We only allow the top two layers to be varied freely. The reciprocal space integration was performed using the the mesh of 2×2×1(Probert et al., 2013) with Gamma-center-off, which was self-consistently selected for total energy minimization. With these special k-points, the total energy is converged to less than 5.0x10-7 eV per atom. The Hellmann-Feynman forces on the atom were converged to less than 0.001 eV/Å.

As to the pseudopotentials, we use the norm-conserving pseudopotentials which can reflect all-electron behavior for outer shell valence electrons for |S-matrix|=1, unlike the ultrasoft pseudopotentials (Hasnip etal., 2006; Laasonen et al., 1993). Therefore, the non-linear core corrected norm-conserving pseudopotential can provide a better response in DFT+U calculations, especially for the calculations of defects (Huang, 2016). We note that our method actually provides almost identical values of the U parameter

for both norm-conserving and ultrasoft pseudopotentials. This means that the obtained value has an intrinsic physical meaning for the studied materials. Meanwhile, this will help us to reflect all-electron behavior of the valence electrons especially for the subtle effect of the 4d electrons and outter 5s electrons. The Ru and Ni norm-conserving pseudopotentials are generated using the OPIUM code in the Kleinman-Bylander projector form (Kleinman and Bylander, 1982), the non-linear partial core correction (Louie et al., 1982) and a scalar relativistic averaging scheme (Grinberg et al., 2000) are used to treat the spin-orbital coupling effect. For this treatment, we similarly choose non-linear core correction technique for correcting the valence-core charge density overlapping in such heavy fermions elements. In particular, we treated the (4d, 5s, 5p) states as the valence states of both Ru and (3d, 4s, 4p) for Ni atoms. The RRKJ method is chosen for the optimization of the pseudopotentials (Rappe et al.,1982).

For all the electronic states calculations on Ru-Ni model, we use the self-consistent determination for the U correction on the localized d orbitals to correct the on-site Coulomb energy of the electron spurious self-energy (Huang, 2017). By that method, the Hubbard U parameters on the half-filled shell of $4d^7$ orbitals of Ru is self-consistently determined to be U_d=2.01 eV, and U_d=5.39 eV for the Ni-$3d^8$, respectively.

Oxygen dissociation

We have also investigated the surface effect on the oxygen dissociation and systematically summarized the physical absorption energies of oxygen on different sites on RuNi (0001) surfaces in both horizon and vertical positions. The results are shown in **Table S6.** From the table, we can clearly see that based on different position of oxygen, the absorption energy can separate into two ranges (shown in **Figure S24**). For oxygen molecule parallel to the surface, the formation energies vary from 0.739 eV to 1.918 eV while the energy range will increase to 4.526 eV to 5.519 eV for oxygen molecule become vertical to the surface.

Apparently, the RuNi (0001) surface shows much stronger tendency to dissociate oxygen when oxygen molecule is parallel to the surface. Oxygen atoms from dissociated oxygen molecule will locate in the nearest two hollow sites after relaxation, which are usually the most stable site for single atom with strongest binding with nearby three metal atoms. RuNi (0001) surface shows evident distortion for oxygen absorption of vertical positions, representing stronger interaction between the surface and the absorbed oxygen molecule. In particular, Ru shows strong interaction with oxygen atoms due to Ru reflects stronger distortion than Ni. Generally, Ru, Ni and bridge top absorption sites reflect the similar trends of formation energies in both parallel and vertical oxygen positions. However, the hollow site shows a distinct phenomenon on oxygen absorption, which has the lowest formation energy in parallel position but the highest formation energy in vertical position. This is might result from the interaction competition of different nearby metal atoms to the oxygen molecule. Ru exhibits the lowest energy cost in vertical position. Interestingly, we find out that when oxygen molecule is vertical above Ru top site, oxygen molecule will become parallel above Ru under the strong interaction from Ru atom. After relaxation, Ru atom will rise from the surface and form stable

bonds with oxygen molecule. To further confirm the interaction, oxygen models of parallel and vertical positions have been built directly on the RuNi (0001) surface with distorted Ru atom and energy results are shown in **Table S7**.

After relaxation, both positions show stable oxygen molecule on the surface with bonding with the distorted Ru atom. However, the absorption energy of parallel position will significantly increase and become close to the vertical position result. We speculate that Ru will consume the energy to interact with oxygen atoms even in vertical position. After distortion, Ru will be oxidic by the oxygen and lose the ability to further dissociate with oxygen molecules. Therefore, we conclude that Ru will play a dominant role in interacting with oxygen related molecules or intermediates.

Detailed comparison for the preliminary absorption behavior on the cubic-RuNi (111) and hcp-RuNi (001) surface

1. Energetics

Without any oxygen preliminary coverage during the pre-annealing treatment, the hydrogen molecules actually undergo a high barrier of dissociation. However, their binding energy is too high, which means the H_2 on the RuNi confirms to be a good desorption with energy of 2.7 eV in binding with the RuNi surface (**Figure S25**).

We further simulate the oxygen partially oxidizing behavior on the RuNi during the pre-annealing treatment experimentally. We found the RuNi surface activity obviously high to perform an evident oxygen molecules cleavage, and therefore, further cause the partial oxidation states with high valence state for Ru and Ni existing on the surface (e.g. Ru^{4+} and Ni^{3+}). More importantly, with the view on the energetics, we confirm that the O-coverage could not proceed infinitely large and exhibit an optimal coverage on this surface. This arises because after a partial O-coverage on the RuNi surface, the O-O bond cleavage could not further be carried out. This indicates the oxygen preliminary coverage that form Ru-O and Ni-O bonding could not continuously occur when the O-O bond cleavage is inhibited. Thus, the OER further desorption performance can be guaranteed with pre-annealing treatment in our experiments, which has been confirmed by our DFT calculations.

ccording to our binding energy calculation, we confirm that oxygen cover on the surface can significantly affect the further absorption behaviors. Several possible combinations of oxygen coverage have been built for illustrating the physicochemical trend, which are ortho-, meta-, and para- positions respectively. We found that the energy barrier for O_2 absorption has been largely decrease. However, the O-O bond cleavage has been further prohibited. Even the absorption energy of O_2 molecule may be further reduced,

while the surface activity increase to a saturation level as shown in the Figure X1b. In Meta- and Para- positions, the suppression of O-O bond dissociation in both O_2 and H_2O are successfully achieved with even lower energy barriers. The binding energy of H is approaching nearly constant independent to the absorption-surface or absorption-site preferences, which denoting a saturated level for highly efficient desorption performance in HER.

2. Electronic structures

We further test the difference of the RuNi surface model with and without partial O-coverage effects. As shown in the total density of states (TDOS, **Figure S26)**, the overall system does not show any substantial difference or contrast in the electronic states especially to the surface levels. Only a minor difference has been noted as the absence of the long-range order of the Ru and Ni sites, as the absence of the van-Hove singularities and spectra-smoothing behavior have been simultaneously observed.

We further on a projected partial density of states (PDOSs) on the RuNi surface to interpret the interplay effect, especially to the d-orbitals of Ru and Ni sites, as well as the adsorbing O-2p orbitals. The PDOS shows an obvious overlapping effect between the surface d-band and O-2p orbital level where the O acts as the stable surface adsorbates **(Figure S26)**. This denotes the Ru and Ni will be rather active to take an open and active site to locate the extrinsic O absorption via the initial O-O cleavage. This self-consistently confirms our above energetic analysis of the O-partial coverage effect on the RuNi, which is energetically preferable.

With more detail, we projected the d-bands with individual contributions from the Ru and Ni sites on the surface, respectively **(Figure S26)**. It is found that the Ru-4d orbital level has substantially clear overlapping effect with adsorbed O-2p orbitals, while only a minor overlapping effect to the Ni-3d orbital level.

This indicates the physical trend that, there has been an evidently stronger electron transfer between Ru-site and adsorbed O-related species on the RuNi surface, especially to the partially O-covered. This can further explain the Ru exhibits higher valence charge states than the one found in Ni sites, which are Ru^{4+} and Ni^{3+} reported in our experimental section of this manuscript.

3. Orbital energetic behaviors

The electronic properties have been described with recently developed ab-initio orbital corrections (Huang, 2016; Huang, 2016; Huang, 2016). The core of the method reflects a generalized searching path towards the optimal parameters valid to exhibits the different chemical bonding information within various materials systems [2, 3]. Here in the work, total energy calculation can be successfully achieved with consideration of the targeted orbital projected under any given case of bonding.

With the on-site orbital potential energy projections on the partially O-covered RuNi surface, we found the nearest neighboring (next to O) Ru and Ni sites have some evident changes different from the pristine RuNi surface. With existence of the oxidation states, a strong charge transfer between Ru/Ni-sites and O adsorbates has been found. Overall, from the projections **(Figure S27)**, they all show the open-shell active effect which means in the RuNi alloy system, the electrons transfer are very active and easy, which has been previously confirmed by our isotropic metallic band structure based on the hexagonal lattice.

As shown in the projections, the Ni-3d orbital exhibits an open-shell effect where the electronic on-site coulomb potential reduces from 5.39 eV to the 1.72 eV (ΔNi= -3.67 eV) indicating an electronic transfer from the original Ni-site to the others, which is the O-site as we confirmed. Meanwhile, a weakened electronic negativity for the Ni-site has been found **(Figure S27)**.

Further on the behavior for the Ru-4d orbital, it is found that the Ru-4d open-shell effect turns to be wider gap compared to the Ni-3d projection, potentially indicating a stronger electron transfer effect between Ru and O than the Ni sites. The on-site electronic Coulomb potential for the Ru-4d changes from 2.01 eV to the 6.38 eV (ΔRu= +4.37 eV) **(Figure S27)** showing a stronger electronic negativity on the Ru site as it stands for the high capabilities in oxidation by further O-coverage. Therefore, the high valence charge states of the Ru^{4+} and Ni^{3+} can be also reflected from our calculations and the calculation self-consistently confirmed their existence, where correlates to the water splitting performance in our experiment.

4. Adsorption analysis

From **Figure 6c**, it is noted that O shows much lower chemisorption energy than other species on the hexagonal surface that can also prove the oxidation states on the surface will be possible to happen. Moreover, we have operated detailed calculations on the RuNi surface with partial oxidation states. Comparing to H or H_2 or H_2O, the chemisorption of O_2 and O atoms is highly favorable and very stable on the surface, which can support that why the concentration of oxidation states is very high **(Figure S28)**. For better comparison and explanation of why oxidation state occurred, we have also operated detailed calculations on the cubic surface to observe the oxidation states. We found the O adsorption formation energy can be further lowered downshift when more O adsorption participates **(Figure S28)**. Therefore, our calculations on the RuNi surface with and without partial oxidation states have been carried out, which will assist us on the interpretation of the mechanism between microscopic behaviors and macroscopic experimental observations. Particularly in the **Figure S28**, it has shown the formation energies of H, 2H, H_2, O, and O_2 on the RuNi surface with partial oxidation. Even though the total energy is larger than the hexagonal phase, the chemisorption energy tendency

between different species is similar. $2H \rightarrow H_2$ is still energetically favorable that facilitate the HER reaction. Oxygen atoms adsorption near the surface shows different behavior. Note that, the binding energy of single oxygen atom on surface is much higher. However, the chemisorption energy of oxygen atom has been significantly decreased to near 0.7 eV, meaning the strong tendency of further 2O chemisorption. The low absorption energy of O_2 supports both $2O \rightarrow O_2$ and O_2 desorption reactions. Therefore, both hexagonal and cubic phase of such Ru-Ni system shows high catalytic reactivity for water splitting based on DFT calculations.

We further compared the O_2 adsorption energy with related to the different percentage of O-coverage (to quantitatively denote the oxidation state coverage rate), in forms of 0% (without coverage), 4.1% (very light coverage), and 12.5% (light coverage). The adsorption energy of O_2 has shown a clear physicochemical down-trend to stabilize on the surface without any O-O bond cleavage **(Figure S28)**. This indicates the oxidation state will promote the stabilities of O_2 on the surface of RuNi system.

REFERENCES

CLARK, S. J., SEGALL, M. D., PICKARD, C. J., HASNIP, P. J., PROBERT, M. I., REFSON, K & PAYNE, M. C. 2005. First principles methods using CASTEP. *Z Kristallogr*, .220, 567-570

VLADIMIR, I. A., ARYASETIAWAN, F & LICHTENSTEIN, A. I. 1997. First-principles calculations of the electronic structure and spectra of strongly correlated systems. *J Phys Condens Matter* 9, 767.

HUANG, B., GILLEN, R & ROBERTSON, J. 2014. Study of CeO_2 and its native defects by density functional theory with repulsive potential. *J Phys Chem C*, 118, 24248-24256.

HUANG, B. 2014. Superiority of DFT+ U with non-linear core correction for open-shell binary rare-earth metal oxides: a case study of native point defects in cerium oxides. *Philos Mag*, 94, 3052-3071.

HUANG, B. 2016. Unraveling energy conversion modeling in the intrinsic persistent upconverted luminescence of solids: a study of native point defects in antiferromagnetic Er_2O_3. *Phys Chem Chem Phys*, 18, 13564-13582.

MARZARI, N., VANDERBILT, D & PAYNE, M. C. 1997. Ensemble density-functional theory for ab initio molecular dynamics of metals and finite-temperature insulators. *Phys Rev Lett*, 79, 1337.

PROBERT M. I. J & PAYNE, M. C. 2003. Improving the convergence of defect calculations in supercells: An ab initio study of the neutral silicon vacancy. *Phys Rev B*, 67, 075204.

HASNIP P. J., PICKARD, C. & COMPUT, J. 2006. Electronic energy minimisation with ultrasoft pseudopotentials. *Phys Commun*, 174, 24-29.

LAASONEN, K., PASQUARELLO, A., CAR, R., LEE, C & VANDERBILT, D. 1993. Car-Parrinello molecular dynamics with Vanderbilt ultrasoft pseudopotentials. *Phys Rev B*, 47, 10142.

KLEINMAN L & BYLANDER, D. M. 1982. Efficacious form for model pseudopotentials. *Phys Rev Lett*, 48, 1425.

LOUIE, S. G., FROYEN, S & COHEN, M. L. 1982. Nonlinear ionic pseudopotentials in spin-density-functional calculations. Phys. Rev. B. 26, 1738.

GRINBERG, I., RAMER, N. J & RAPPE, A. M. 2000. Transferable relativistic dirac-slater pseudopotentials. *Phys Rev B*, 62, 2311.

RAPPE, A. M., RABE, K. M., KAXIRAS, E & JOANNOPOULOS, J. D. 1990. Optimized pseudopotentials. *Phys Rev B*, 41, 1227.

HUANG, B. 2017. The screened pseudo-charge repulsive potential in perturbed orbitals for band calculations by DFT+ U. *Phys Chem Chem Phys*, 19, 8008-8025.

HUANG, B. 2016. Intrinsic deep hole trap levels in Cu2O with self-consistent repulsive Coulomb energy. *Solid State Commun*, 230, 49-53.

HUANG, B. 2016. Strong compensation hinders the p-type doping of ZnO: a glance over surface defect levels. *Solid State Commun*, 237, 34-37.

HUANG, B. 2016. 4f fine‑structure levels as the dominant error in the electronic structures of binary lanthanide oxides. J Comput Chem, 37, 825-838.